Supplementary Information

Gas-liquid switching reaction system for normothermic photo-driven chemical looping ammonia synthesis

Yunfan He,[ab] Lulu Zhang,[c] Fangfang Li,[ab] Jianxin Liu,[*a] Rui Li[*a] and Jiancheng Wang[*ab]

a.Shanxi Key Laboratory of Complex Air Pollution Control and Carbon Reduction, College of Environmental and Ecology, Taiyuan University of Technology, Taiyuan 030024, PR China.

b.College of Chemical Engineering and Technology, Taiyuan University of Technology, Taiyuan 030024, PR China.

c.Department of Materials and Chemical Engineering, Taiyuan University, Taiyuan, 030032, PR China.

*Corresponding author: Jianxin Liu Email: liujx0519@163.com

*Corresponding author: Rui Li Email: lirui13233699182@163.com

*Corresponding author: Jiancheng Wang Email: wangjiancheng@tyut.edu.cn

1. Characterization. The X-ray diffraction (XRD) pattern of the sample was characterized using the Dmax-2500 Phaser with Cu/K radiation, scanning in the range of 10°-80° at a rate of 5°/min. X-ray photoelectron (XPS) spectroscopy was measured using the Thermo Scientific K-Alpha, calibrated to the binding energy of all peaks through the C1s peak (284.6 eV) at a voltage of 12 kV and an operating current of 6 mA. Transmission electron microscope (TEM) images were taken using the Japanese JEOL JEM-F200 at an accelerating voltage of 200 kV. Scanning electron microscopy (SEM) testing was conducted using the Czech TESCAN MIRA LMS, with an accelerating voltage of 10 kV. Raman was carried out using a Renishaw Raman microscope inVia™ Qontor® (Renishaw, Inc. Hoffman Estates, IL). In-situ diffuse reflectance Fourier transform infrared spectroscopy (in-situ DRFTIRS) was recorded using an in-situ FTIR spectrometer (Tensor 2, Bruker, Germany), a Pike DRIFTS sample cell, and a high-precision MCT detector cooled with liquid nitrogen. Electron paramagnetic resonance (EPR) testing was completed using the German Bruker EMXplus-6/1 EPR spectrometer. Photoluminescence (PL) spectra were measured using the Edinburgh instrument FLS980 Series of Fluorescence Spectrometers. N_2 program temperature desorption (N_2-TPD) testing was performed using the British Hiden DECRA. UV-vis diffuse reflectance spectroscopy (UV-vis-DRS) was measured using the UH4150 spectrophotometer (Hitachi, Japan) with $BaSO_4$ as a reference sample.

2. Photoelectrochemical measurements. Cyclic voltammetry (CV), Linear sweep voltammetry (LSV), Electrochemical impedance spectroscopy (EIS), photocurrents,

and Mott-Schottky testing were all carried out on a CHI-660E electrochemical workstation (Shanghai Chenhua, China) with a three-electrode system.

3. Reactivity measurement. The activity of the sample was tested by photocatalytic nitrogen fixation in a quartz glass reactor. Place the 300W Xe lamp, which simulates sunlight, vertically outside the reactor. All water used in the experiments was deionized water, with a measured pH of 6.55 ± 0.04. All activity data reported in this work are derived from three independent replicate measurements.

Photocatalytic activity testing of the PCALS. In the GR (gas-solid reaction) step, 4 mg photocatalyst was dissolved in 0.2 mL Et, and put into an ultrasonic washer for 30 minutes. Then apply the solution evenly onto the PP film. The photocatalytic activity reaction was carried out in a quartz glass reactor, and the film was placed on the bottom of the reactor without any water. And feed N_2 containing saturated water vapor into the reactor at a flow rate of 80 mL·min^{-1}, use 10 mL 0.1M H_2SO_4 solution at the tail for receiving ammonia. Finally, use a UV visible spectrophotometer to detect the concentration of $NH_4^+$with Nessler's reagent at 420 nm.

In the LR (liquid-solid reaction) step, upon completion of the GR step, the PP membrane was rinsed with deionized water and subsequently dried in a vacuum oven at 60 °C. The dried membrane was then immersed in 100 mL of deionized water, and N_2 was purged through the reactor at a flow rate of 80 mL min^{-1} for 0.5 h to eliminate air. After the reaction, the resulting solution was centrifuged at 8000 rpm for 10 min, and the supernatant was collected. The NH_4^+ concentration in a 10 mL aliquot of the supernatant was then measured using a UV-vis spectrophotometer with Nessler's

reagent at 420 nm.

Photocatalytic activity testing of the single GR step. The activity testing procedure for an isolated GR step follows the same protocol as that employed for the GR step within the PCLAS process.

Photocatalytic activity testing of the single LR step. 4 mg of TiO_2 was dispersed in 100 mL of distilled water. The suspension was continuously stirred while N_2 was purged through the solution at a flow rate of 80 mL min^{-1} for 0.5 h, after which simulated solar irradiation was applied. Following the reaction, the resulting solution was centrifuged at 8000 rpm for 10 min, and the supernatant was collected. The NH_4^+ concentration in a 10 mL aliquot of the supernatant was then measured using a UV-vis spectrophotometer with Nessler's reagent at 420 nm.

Universality tests. Photocatalytic activity testing of PCLAS. In the GR step, 4 mg photocatalyst was dissolved in 0.2 mL Et, and put into an ultrasonic washer for 30 minutes. Then apply the solution evenly onto the PP film. The photocatalytic activity reaction was carried out in a quartz glass reactor, and the film was placed on the bottom of the reactor without any water. And feed N_2 containing saturated water vapor into the reactor at a flow rate of 80 mL·min^{-1}, use 10 mL 0.1M H_2SO_4 solution at the tail for receiving ammonia. Finally, use a UV visible spectrophotometer to detect the concentration of $NH_4^+$with Nessler's reagent at 420 nm.

In the LR step, upon completion of the GR step, the PP membrane was rinsed with deionized water and subsequently dried in a vacuum oven at 60 °C. The dried membrane was then immersed in 100 mL of deionized water, and N_2 was purged

through the reactor at a flow rate of 80 mL min^{-1} for 0.5 h to eliminate air. After the reaction, the resulting solution was centrifuged at 8000 rpm for 10 min, and the supernatant was collected. The NH_4^+ concentration in a 10 mL aliquot of the supernatant was then measured using a UV-vis spectrophotometer with Nessler's reagent at 420 nm.

Photocatalytic activity testing of PAS. The experiments were conducted at a constant temperature of 25 °C. Specifically, 4 mg of metal oxide (MoO_3, NiO, ZrO_2, Y_2O_3, Gd_2O_3, Bi_2O_3, Co_3O_4, CuO, In_2O_3, MgO) was dispersed in 100 mL of distilled water. The suspension was continuously stirred while N_2 gas was bubbled through at a flow rate of 80 mL·min^{-1} for 0.5 h to establish the reaction atmosphere and purge any residual air, after which simulated solar irradiation was applied. Upon completion of the reaction, the solution was centrifuged at 8000 r/min for 10 min, and the supernatant was collected. Subsequently, a 10 mL aliquot of the supernatant was analyzed for NH_4^+ concentration using a UV-vis spectrophotometer with Nessler's reagent at 420 nm.

Determination of NH_3 in the gas phase above the LR solution. Upon completion of the LR step, the reactor was sealed, and N_2 gas was purged through the solution at a flow rate of 80 mL min^{-1} for 45 min. The exhaust gas was passed into a 0.1 M H_2SO_4 solution as an absorbent. Following the purging step, the absorbent was centrifuged at 8000 r min^{-1} for 10 min. The NH_4^+ concentration in 10 mL of the supernatant was then measured using a UV-vis spectrophotometer with Nessler's reagent at 420 nm.

As shown in Fig. S12, the three independent experiments yielded absorbance values at 420 nm of 0.01231, 0.00854, and 0.00708, respectively. Based on the Nessler's

standard calibration curve presented in Fig. S4, these results confirm the absence of NH_3 in the exhaust gas from the LR step.

To minimize the possibility of experimental error, the analyzed samples were synthesized multiple times for this study, and each sample was triplicated for the photocatalytic performance of ammonia synthesis.

4. Density functional theory (DFT) theoretical calculation. The study utilized Density Functional Theory (DFT) based on Cambridge Sequential Total Energy Package (CASTEP) to compute the pathways for PCLAS reactions. Exchange-correlation interactions were determined using the Perdew-Burke-Ernzerhof (PBE) functional within the general gradient approximation (GGA). The dispersion interactions between the adsorbate and substrate were enhanced through the application of the van der Waals correction (DFT-D) method. Kohn-Sham wave functions were expanded in plane waves with a cutoff energy of 450 eV. The special k-point sampling set was employed to approximate the Brillouin zone integration using a 2×1×1 mesh. The convergence criteria for energy and maximum force were set at 1.0×10^{-5} eV/atom and 0.02 eV/Å, respectively. The substrate was modeled with a 20 Å vacuum thickness in the z-direction. The alteration in free energy during the PCLAS process was evaluated using the computational hydrogen electrode (CHE) model.

5. Radial distribution function (RDF) calculation. Molecular dynamics (MD) simulations were conducted to investigate the filling of Ovs in catalysts across various environments, employing the Amorphous Cell model within the Condensed-phase Optimized Molecular Potentials for Atomistic Simulation Studies II (COMPASSII)

force field and Ewald summation method. The total density of gas molecules was set at 2.000 g/cc with an energy accuracy of 0.001 kcal/mol and a buffer zone width of 0.5 Å under the condition of a temperature bias of 298K.

In the GR step, the catalyst is encapsulated within a nitrogen atmosphere containing water vapor, with the vapor pressure determined by the Antoine equation:

$$Log(P) = A - \frac{B}{C + T} \quad (1)$$

Based on the Antoine parameters from the National Institute of Standards and Technology (NIST) database (A = 8.07, B = 1730.63, C = 233.43), the vapor pressure of water (P) is determined to be 3.16 kPa. Given that the GR employs a continuous reaction mode, the total pressure inside the reactor is maintained at 1 atm. Consequently, the molecular ratio of H_2O to N_2 is equivalent to their respective partial pressure ratio:

$$\frac{n_{H2O}}{n_{N2}} = \frac{P_{H2O}}{P_{N2}} \quad (2)$$

The calculated molecular ratio is n_{H2O}:n_{N2} = 2:98. To balance computational accuracy with hardware limitations, the maximum number of solvent molecules in the molecular dynamics simulations was capped at 100. Accordingly, 2 H_2O molecules and 98 N_2 molecules were placed on the TiO_2 surface.

In the LR step, the catalyst is encapsulated in water saturated with dissolved N_2. The solubility of N_2 in water at 25 °C is determined by the following equation:

$$C = \frac{P_{N2}}{k_H} \quad (3)$$

Where P_{N2} represents the partial pressure of nitrogen in air (0.78 atm), and k_H is the

Henry's constant for N_2 in water at 25 °C (1600 atm L mol^{-1}). The solubility is thus determined to be C = 0.000488 mol L^{-1}. Accordingly, the ratio of the number of water molecules per unit volume is calculated as follows:

$$n_{H2O} = \frac{\rho_{H2O}}{M_{H2O}} \quad (4)$$

The calculated concentration of H_2O molecules per unit volume is 55.51 mol, yielding a theoretical n_{H2O}:n_{N2} = 113750:1. Due to the computational constraints on the maximum number of solvent molecules in molecular dynamics simulations, this ratio was adjusted to 99:1. Notably, this approximation results in a significantly higher number of N_2 molecules than under realistic conditions, it does not compromise the conclusion regarding the limited N_2 distribution on the TiO_2 surface in the LR model. Finally, RDF analysis was employed to quantify the distribution of H_2O and N_2 molecules within a distance of 7 Å from the surface.

6. Calculation of apparent quantum (AQY). The AQY is determined by the following equation.

$$AQY = \frac{electrons\ transferred}{incident\ photon} \times 100\% \quad (5)$$

7. Calculation of Solar to Ammonia (STA) conversion efficiency. The STA efficiency is determined by the following equation:

$$STA = \frac{\gamma_H \times \Delta G_r}{I_{light} \times A} \quad (6)$$

where γ_{NH3} denotes the reaction rate (1.64 × 10^{-9} mol s^{-1}), ΔG_r is the Gibbs free energy of the reaction (339000 J mol^{-1}, NIST Chemistry WebBook), I_{light} represents the light intensity (0.035 W cm^{-2}), and A corresponds to the illuminated area (4 cm^2). From these

parameters, the STA efficiency is calculated to be 0.40%.

8. Supporting Figures

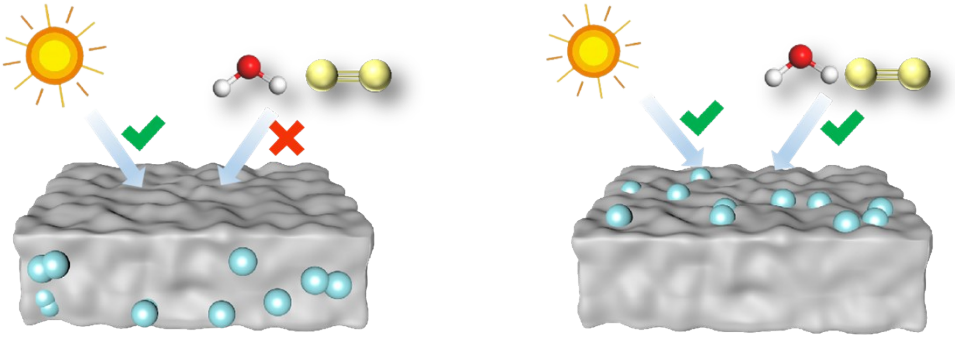

Fig. S1. The optimal configuration of the photocatalytic membrane.

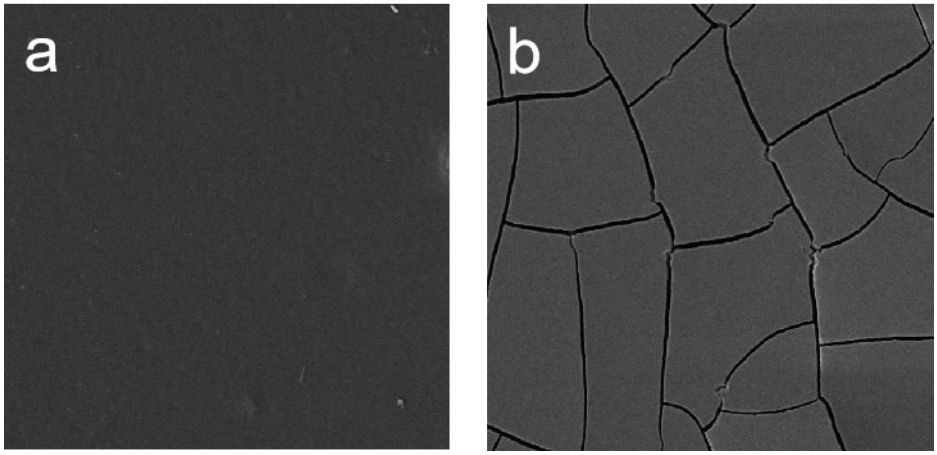

Fig. S2. SEM photo of the surface of (a) bare PP membrane and (b) TPM.

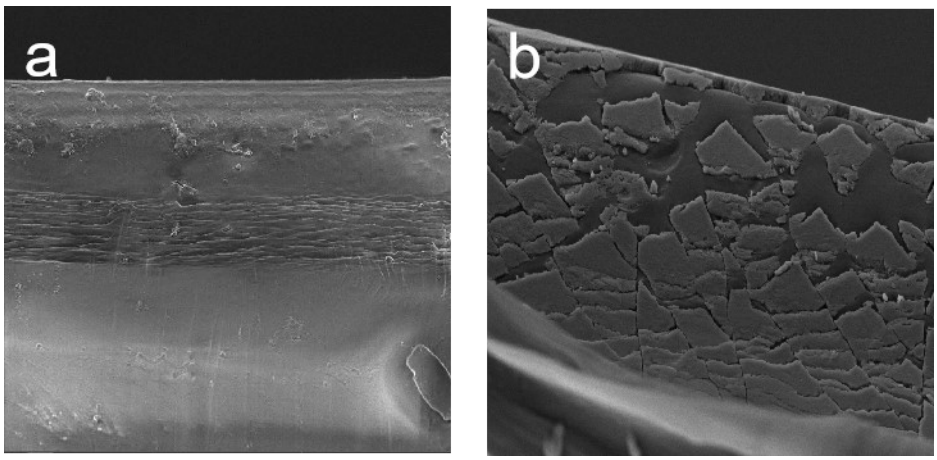

Fig. S3. SEM photo of the interior of the PP membrane and TPM.

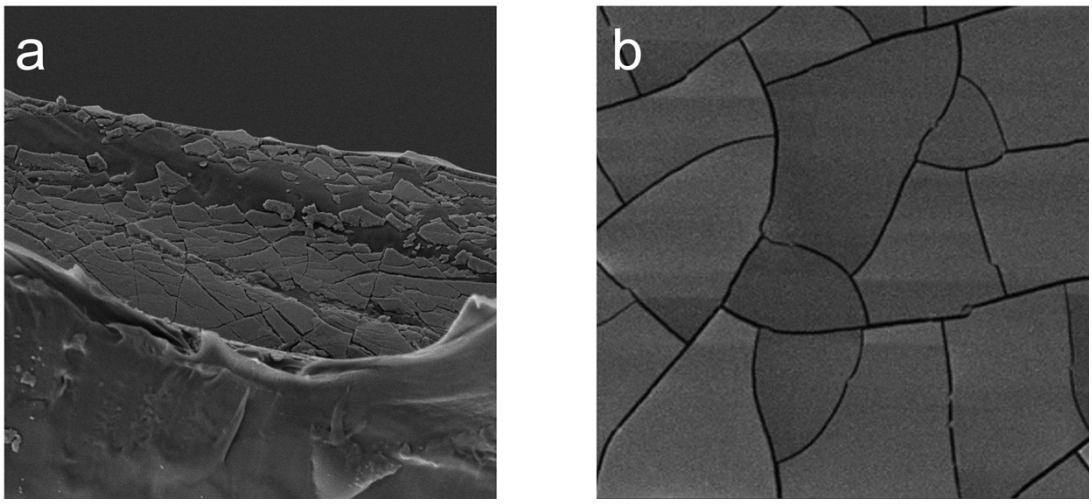

Fig. S4. SEM photo of (a) surface and (b) interior of TPM after ten complete reactions.

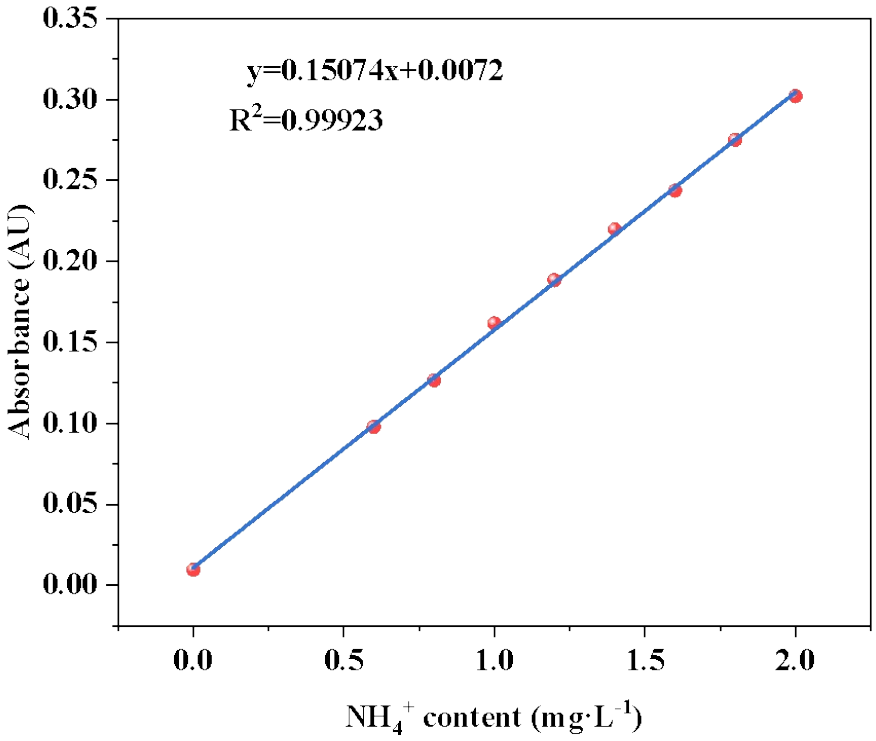

Fig. S5. Nessler's measurement method standard curve.

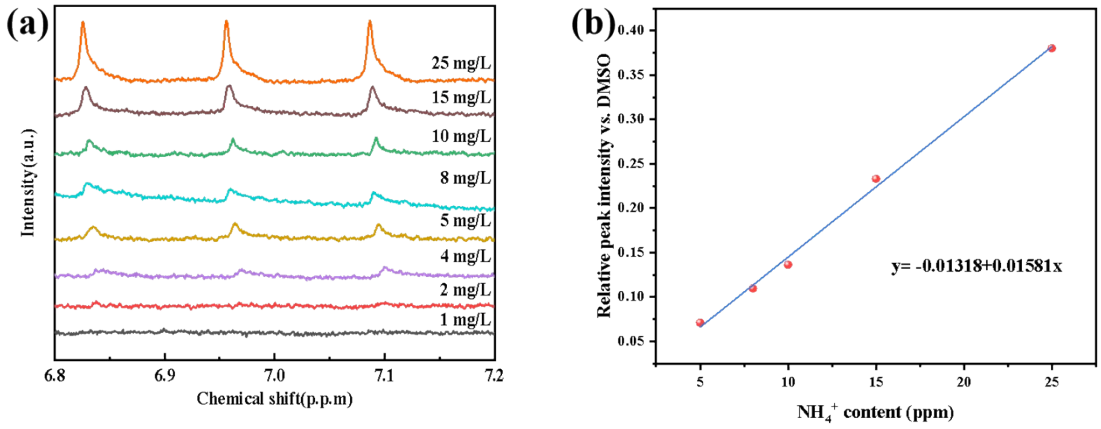

Fig. S6. NMR measurement method standard curve.

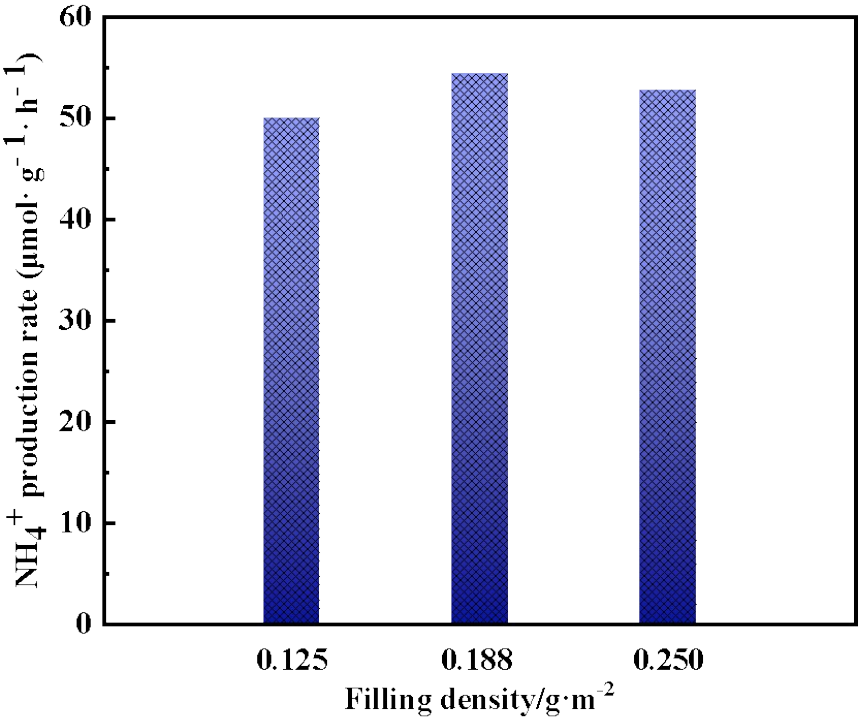

Fig. S7. Ammonia yield of different filling density.

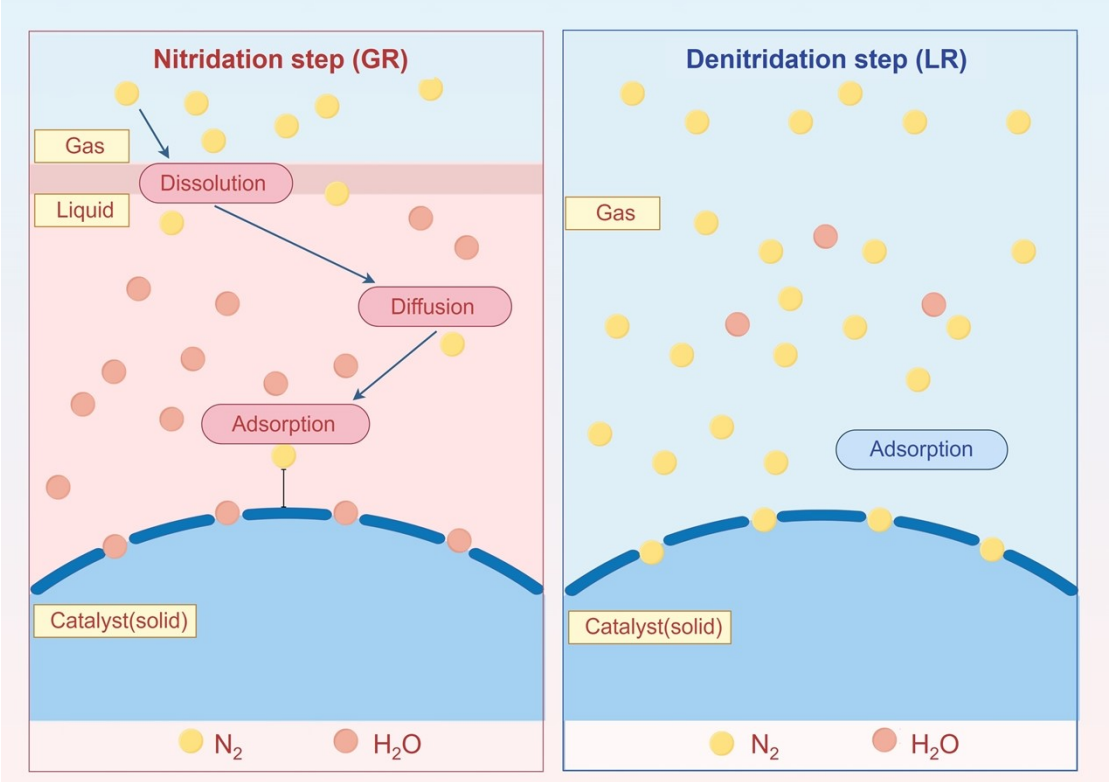

Fig. S8. Schematic diagram of (a) nitridation step and (b) denitridation step.

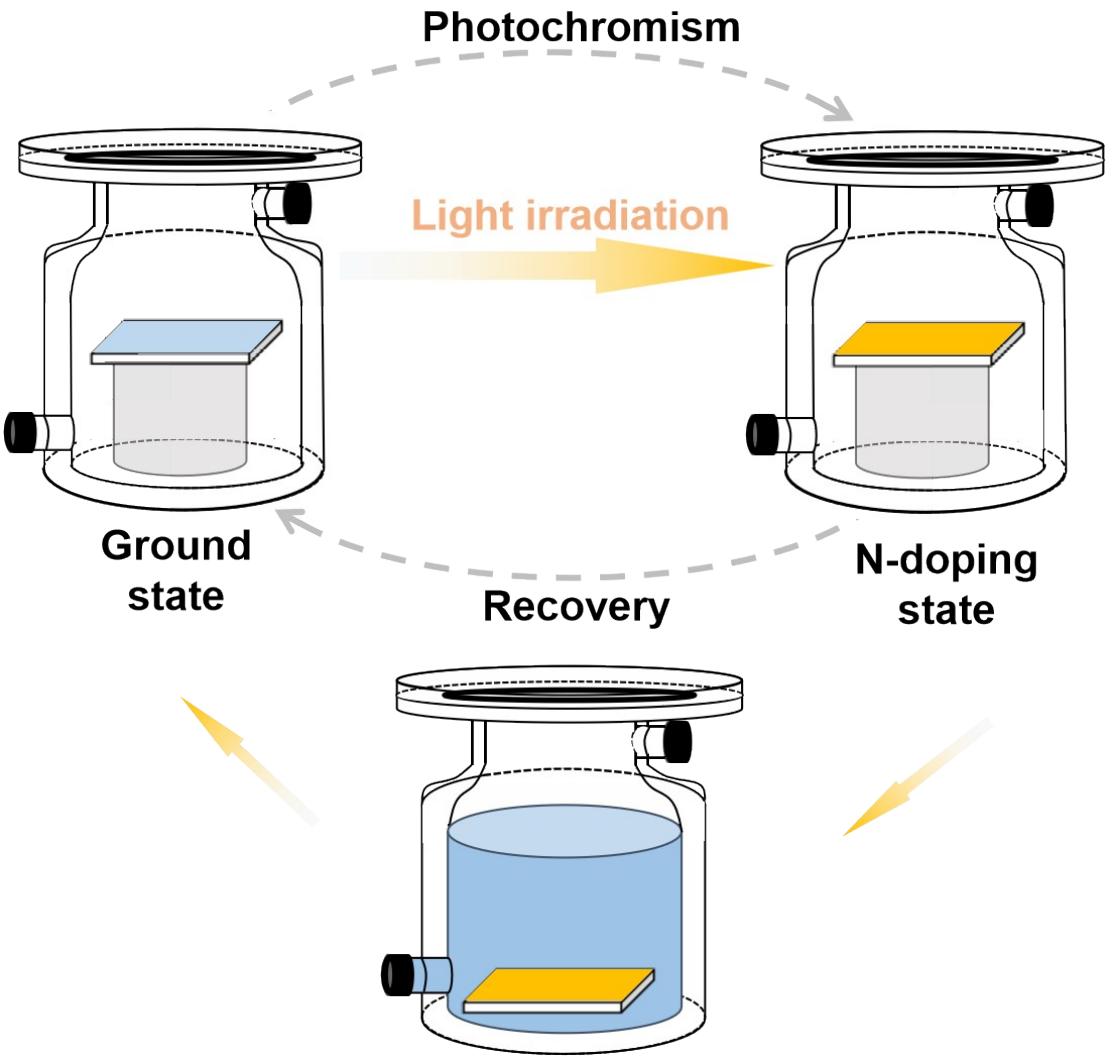

Fig. S9. Experimental setup of PCLAS.

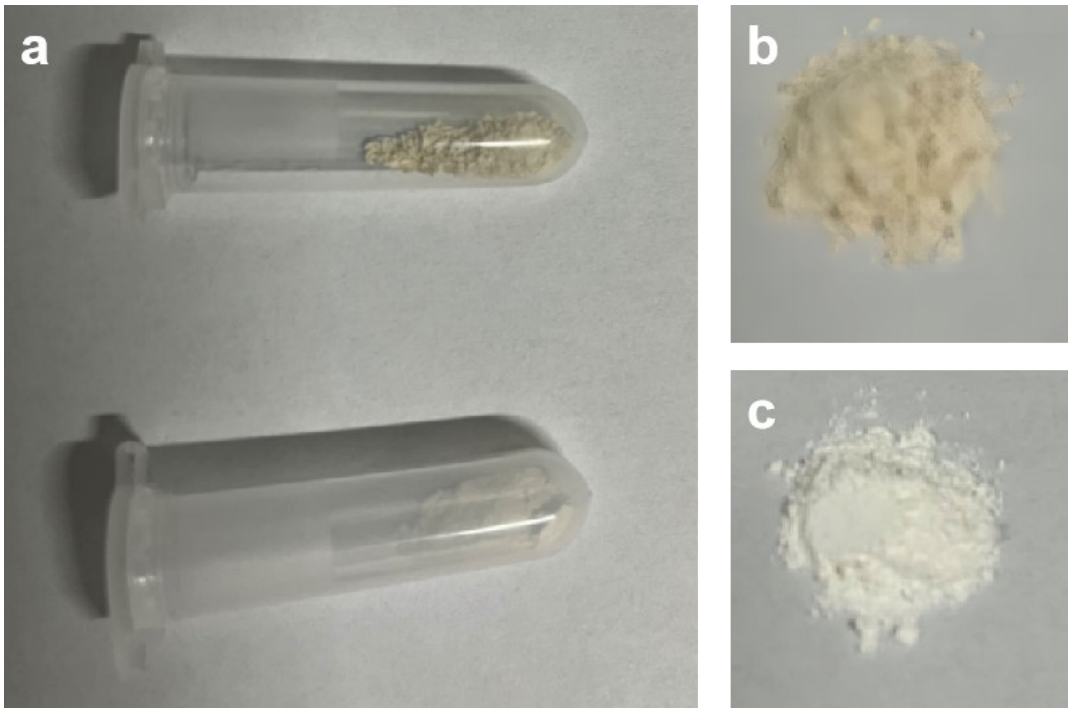

Fig. S10. Photo of nitrogen doping TiO_2 (upper part of a and b), and fresh TiO_2 (lower part of a and c).

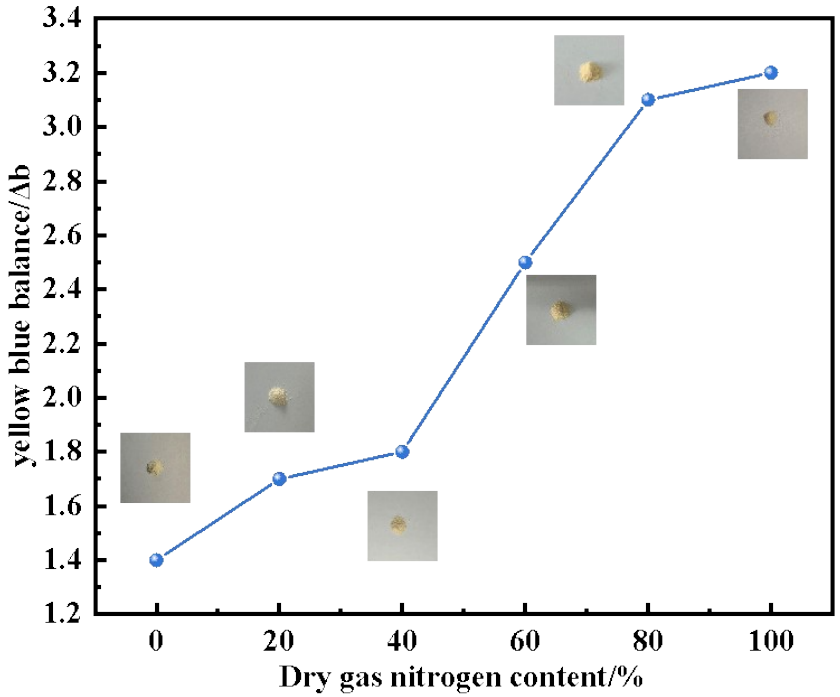

Fig. S11. The formation of nitrogen doping TiO_2 in different N_2 content.

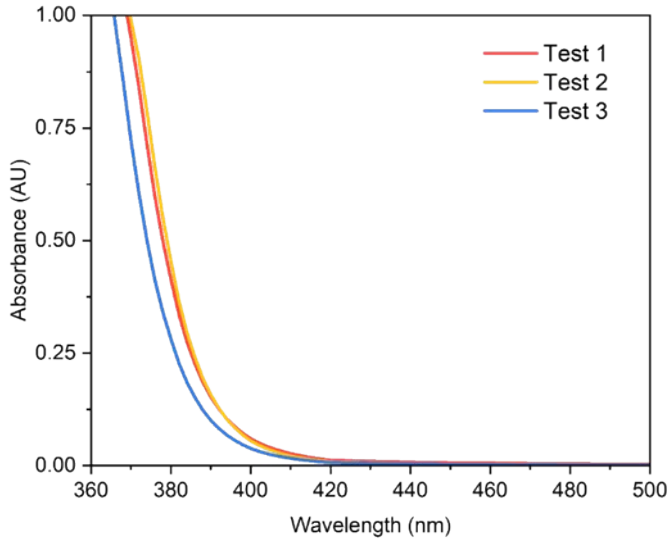

Fig. S12 Determination of NH_3 in the exhaust gas of the LR step using Nessler's method, error bars represent the standard deviation derived from three independent replicate measurements.

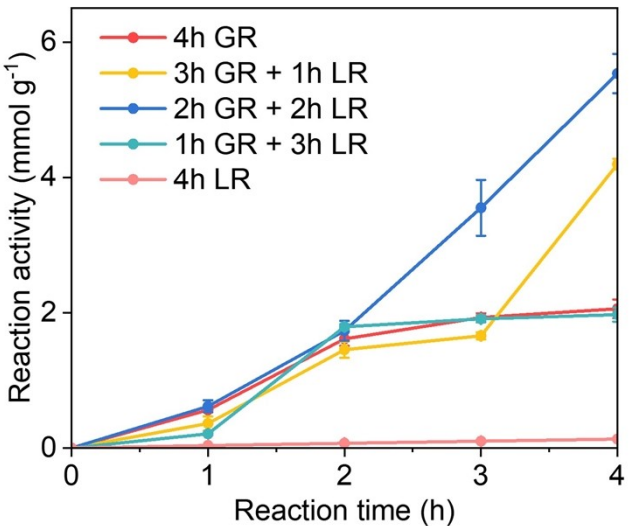

Fig. S13. Ammonia production over TiO_2 as a function of different reaction time allocation schemes: 4h GR, 3h GR + 1h LR, 2h GR + 2h LR, 1h GR + 3h LR, and 4h LR. Error bars represent the standard deviation derived from three independent replicate measurements.

Fig. S13 illustrates the ammonia production performance under various time allocation schemes. A single GR reaction facilitates sufficient catalyst-N_2 contact, delivering an initial activity of 0.92 mmol g^{-1} h^{-1} within the first 2 hours. However, the progressive accumulation of N-doped TiO_2 ultimately leads to catalyst deactivation. A similar deactivation trend is observed for the 3h GR + 1h LR configuration. In this case, the insufficient LR duration precludes the complete release of lattice-bound N atoms, resulting in a diminished overall activity (1.05 mmol g^{-1} h^{-1}). In contrast, the 2h GR + 2h LR configuration not only circumvents catalyst deactivation but also achieves adequate surface nitridation, thereby enabling efficient denitrification. This configuration yields a high activity of 1.48 mmol g^{-1} h^{-1}, confirming its optimality. For the 1h GR + 3h LR configuration, insufficient surface nitridation fails to fully activate the self-activation effect (Fig. S45), leading to low GR activity. Furthermore, the limited quantity of N atoms stored in the lattice cannot sustain the subsequent LR step, causing the overall activity to decrease to 0.49 mmol g^{-1} h^{-1}. The single LR reaction exhibits the lowest activity (0.03 mmol g^{-1} h^{-1}), attributable to the poor solubility of N_2 in water, which restricts effective catalyst-N_2 contact.

Collectively, the 2h GR + 2h LR time ratio represents the optimal configuration, as it leverages the self-activation effect to store abundant N within the lattice while preventing catalyst deactivation arising from excessive surface nitridation.

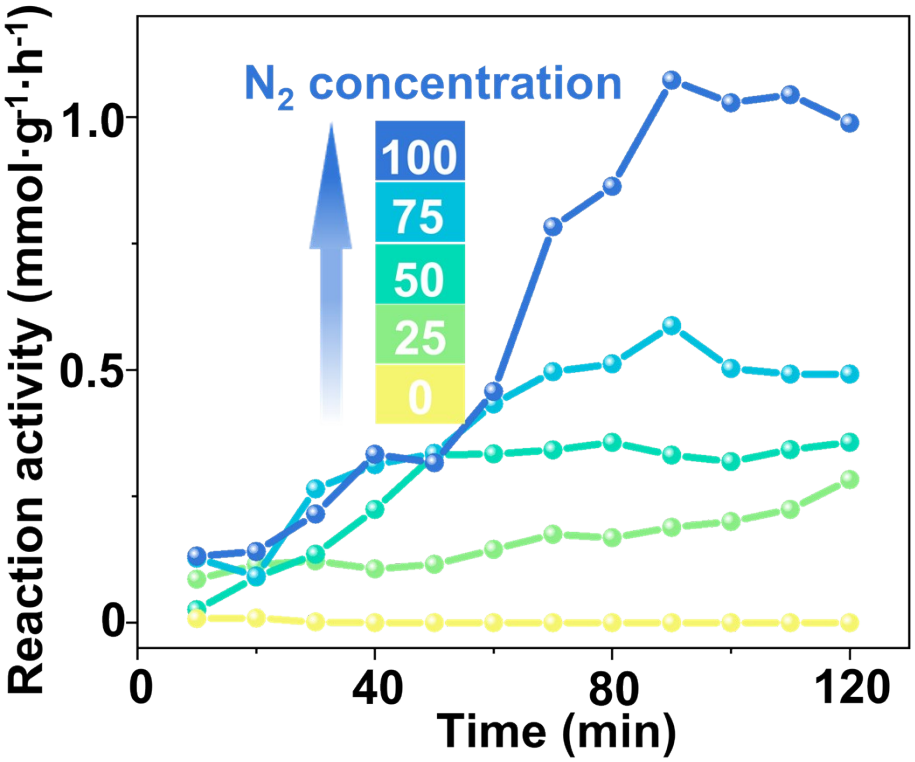

Fig. S14. Self-activation behavior of TiO_2 in GR under irradiation. This effect is attributed to the formation of N-doped TiO_2 on the surface during the reaction process.

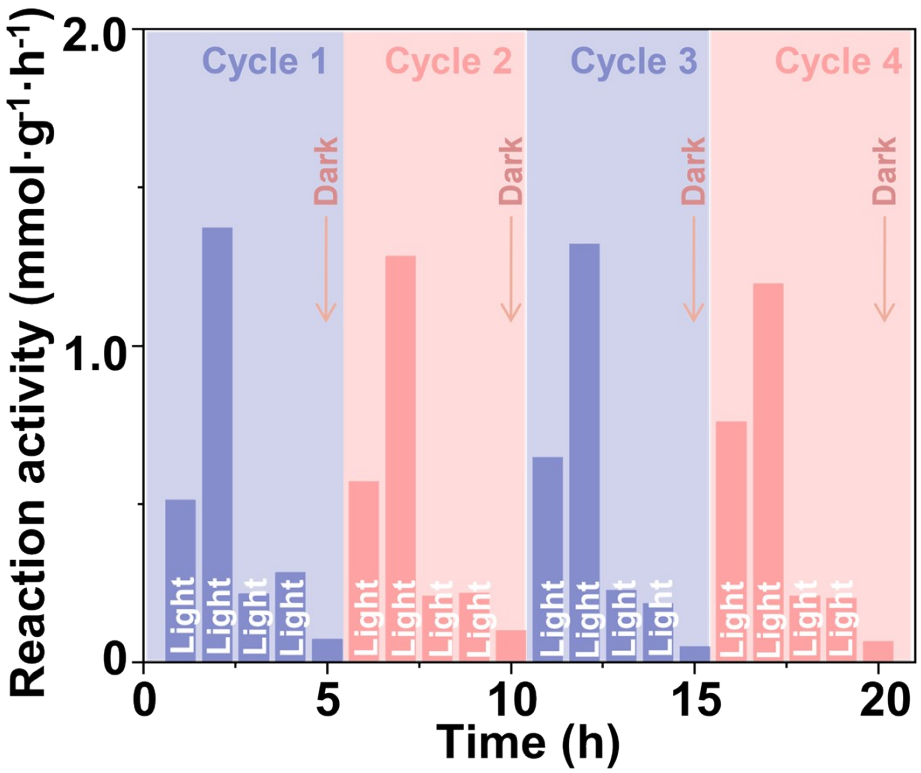

Fig. S15. Photo-memory behavior of TiO_2 under irradiation. This phenomenon is hypothesized to result from the partial hydrogenation and subsequent escape of lattice N atoms under dark conditions.

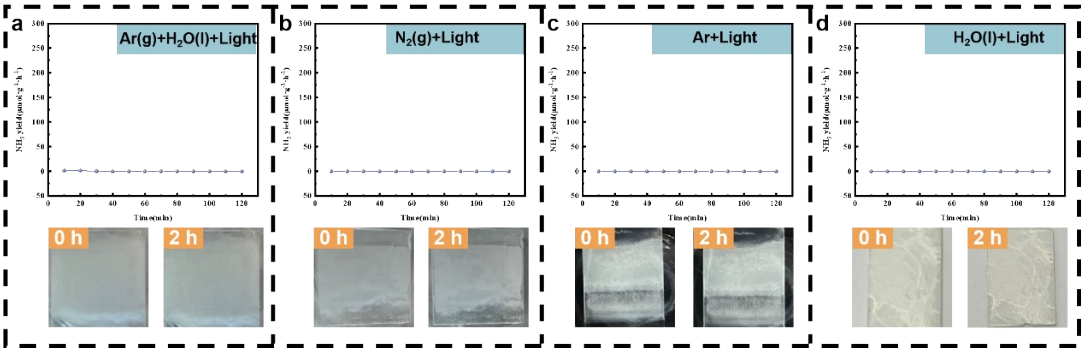

Fig. S16. Comparative experiments in different environments.

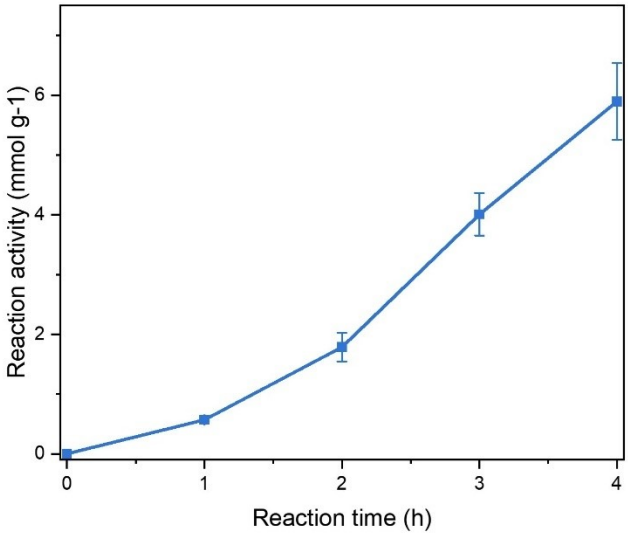

Fig. S17. Ammonia yield of PCLAS (Ar atmosphere in the LR step).

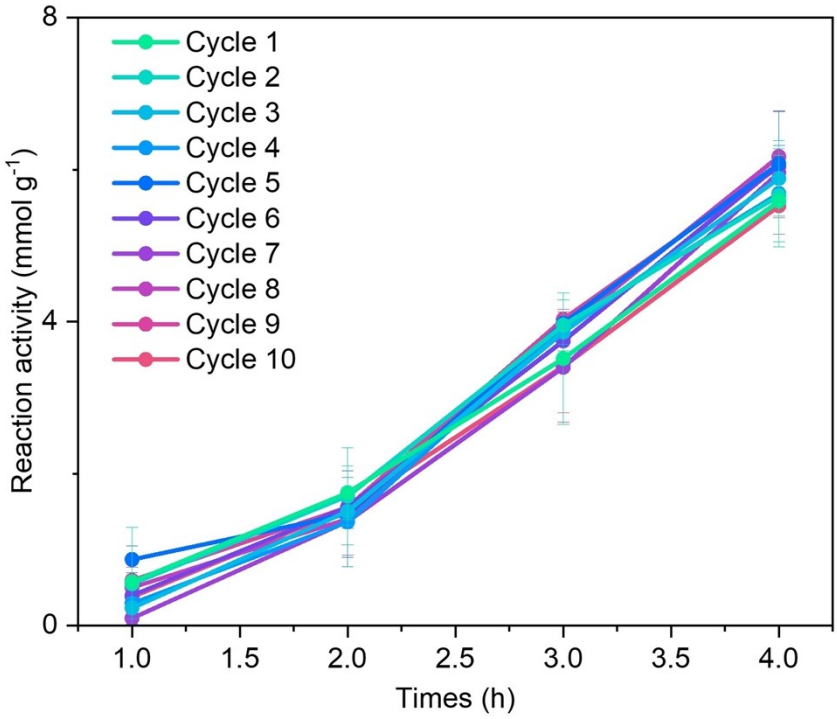

Fig. S18. Persistence test with 10 cycles, error bars represent the standard deviation derived from three independent replicate measurements.

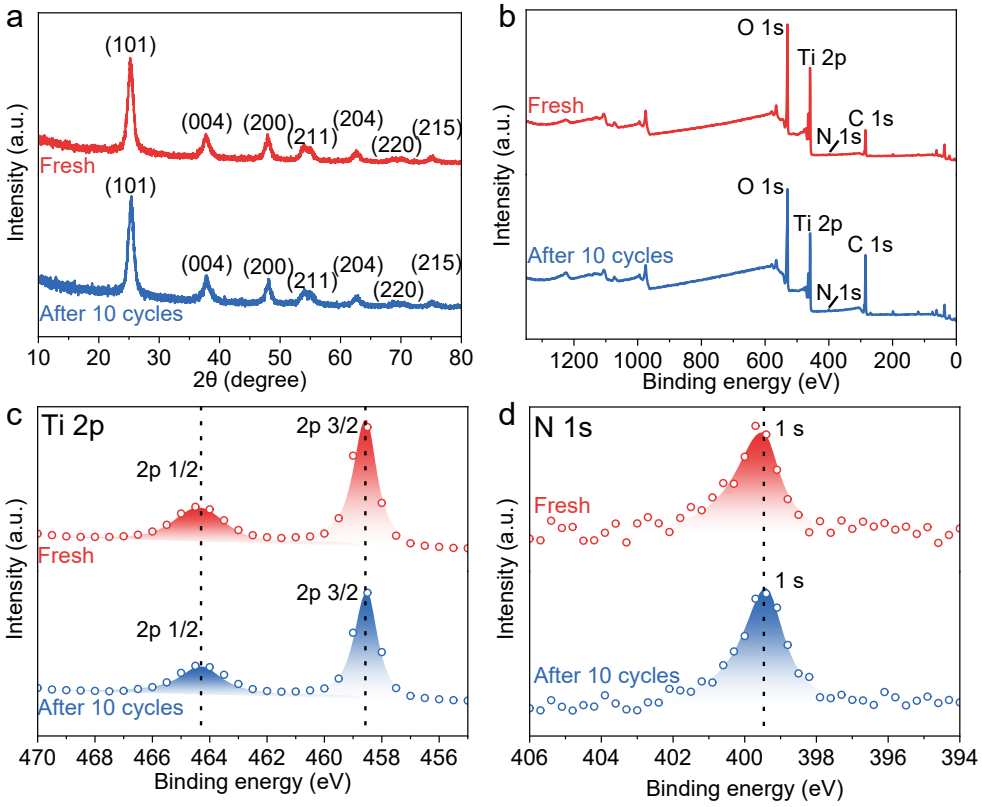

Fig. S19. XRD and XPS spectra of fresh TiO_2 and TiO_2 after 10 cycles.

As illustrated in Fig. S19(a), the crystal structure of TiO_2 remains unchanged after the reaction. In addition, the surface chemical state is well preserved, with no detectable titanium nitride species observed (Fig. S19(b-d)). Collectively, these characterizations confirm the stable performance of this system over ten consecutive cycles.

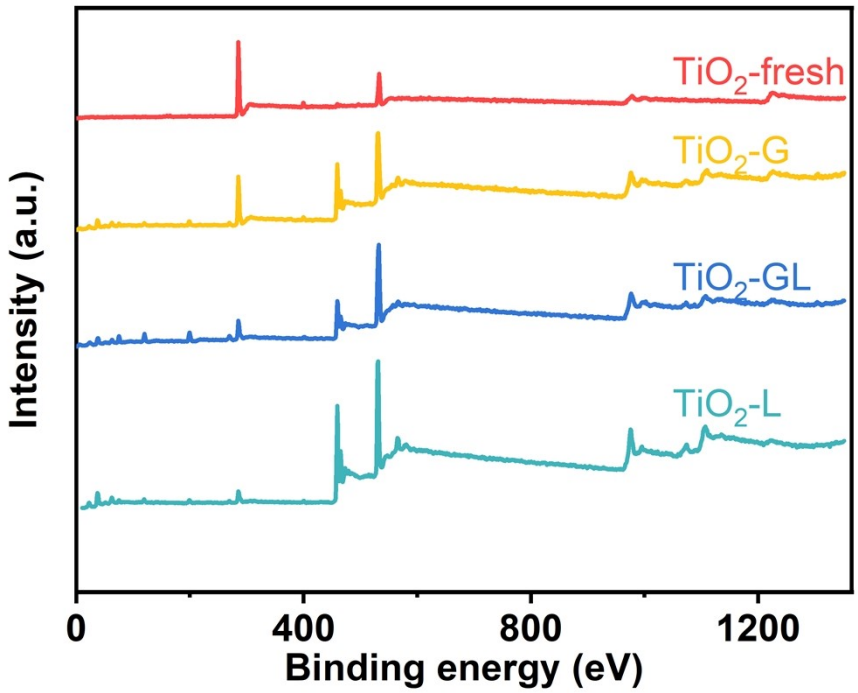

Fig. S20. XPS survey spectra of TiO_2-fresh, TiO_2-G, TiO_2-GL, and TiO_2-L.

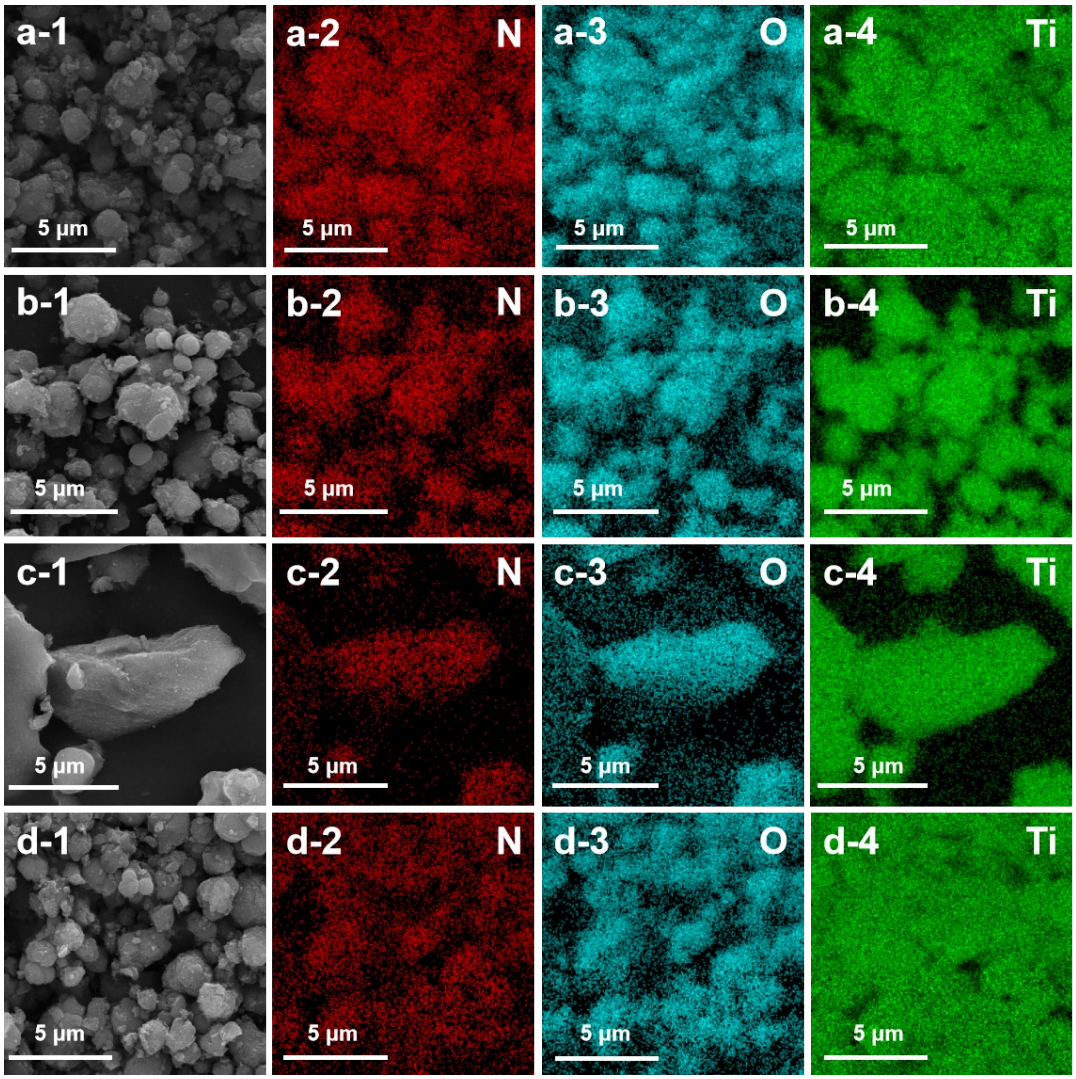

Fig. S21. SEM photo of (a) TiO_2-fresh, (b) TiO_2-G, (c) TiO_2-GL, and (d) TiO_2-L.

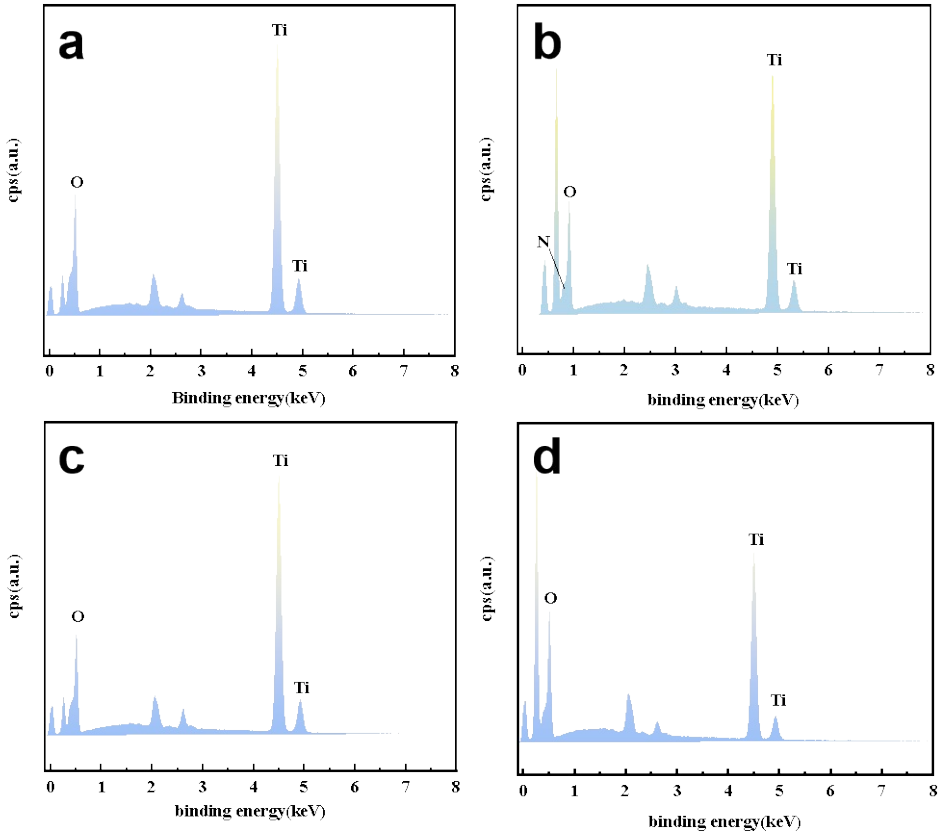

Fig. S22. EDS semi-quantitative spectrogram of (a) TiO_2-fresh, (b) TiO_2-G, (c) TiO_2-GL, and (d) TiO_2-L.

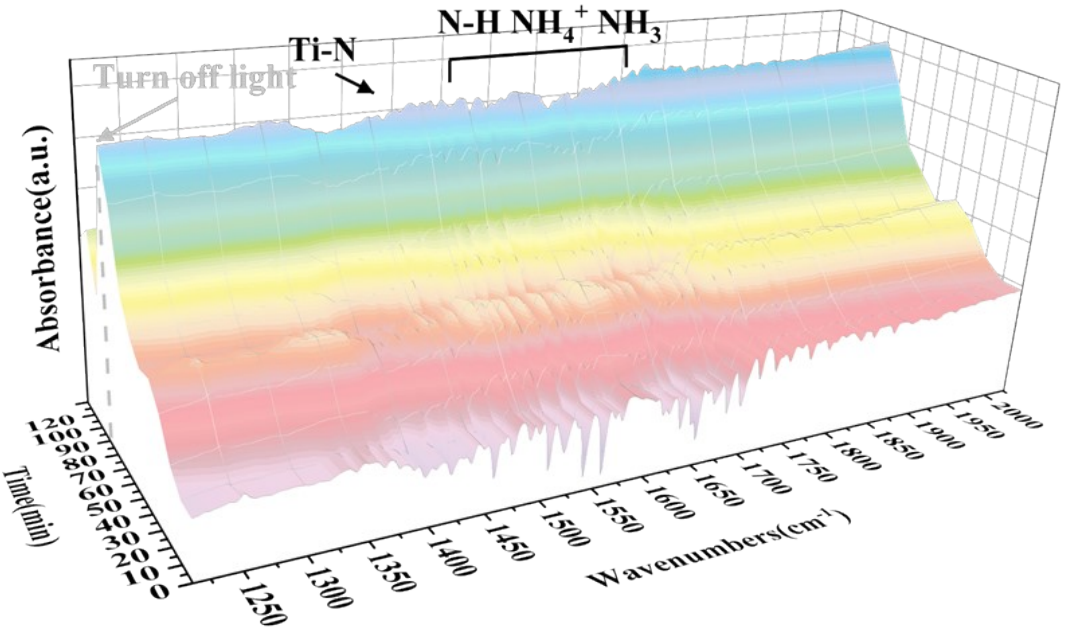

Fig. S23. Full spectrum of in-situ FTIR.

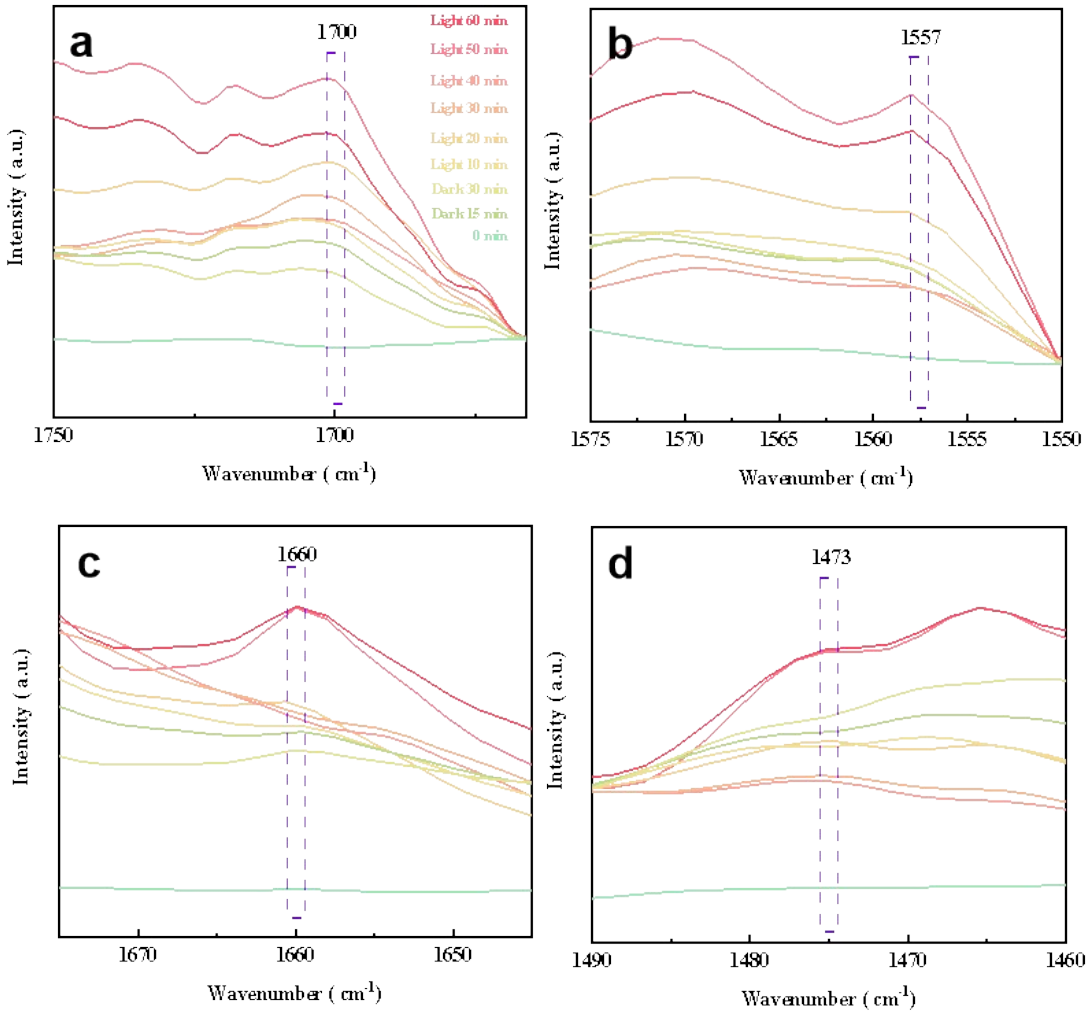

Fig. S24. Single peak magnified image of (a) 1700 cm^{-1}, (b) 1557 cm^{-1}, (c) 1600 cm^{-1}, (d) 1473 cm^{-1}.

Under GR conditions, the contact between the catalyst, nitrogen, and water vapor leads to a gradual enhancement in the range of 1750 cm^{-1} to 1450 cm^{-1}, including the bending and stretching vibrations of the σ(N-H) bonds at 1700 cm^{-1} and 1557 cm^{-1} shown in (a) and (c). These two signal peaks gradually increase and reach a stable state, indicating the chemical adsorption and hydrogenation of N_2 on the catalyst surface during the reaction process.[1,2] At room temperature, the adsorption of ammonia can be divided into two types: the binding of NH_3 at Lewis acid sites and the adsorption of NH_4^+ at Brønsted acid sites.[3,4] The peaks at 1660 cm^{-1} (c) and 1473 cm^{-1} (d) can be respectively associated with the gradual increase of these two adsorption forms.

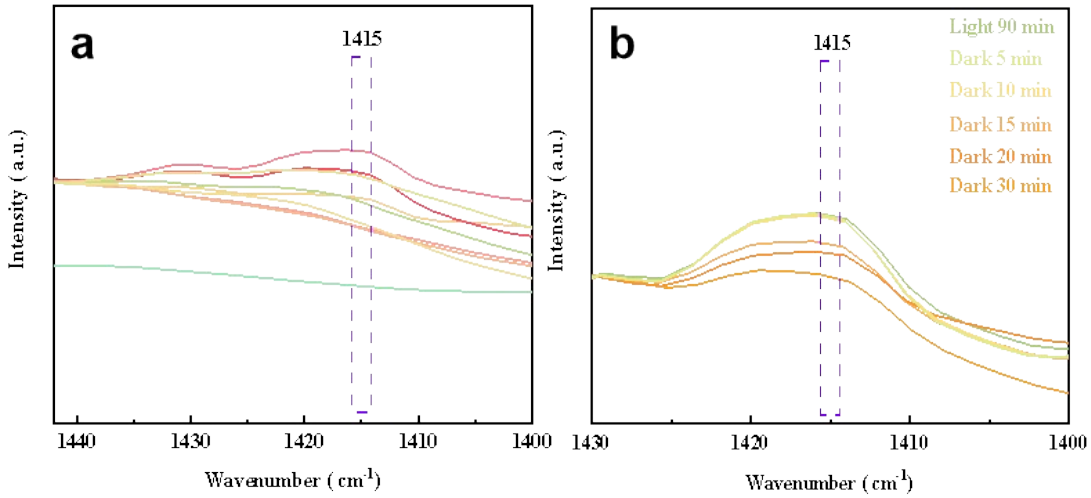

Fig. S25. Single peak magnified image of 1415 cm^{-1}.

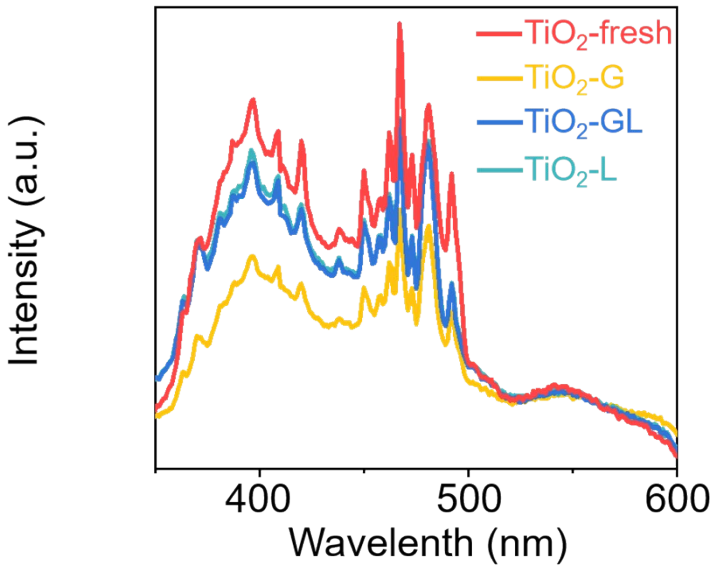

Fig. S26. PL spectrum of TiO_2-fresh, TiO_2-G, TiO_2-GL, and TiO_2-L.

Photoluminescence (PL) analysis indicates that the samples exhibit distinct anatase absorption peaks at approximately 390 nm and 465 nm. Notably, the TiO_2-G sample demonstrates lower peak intensity than the TiO_2-fresh, TiO_2-GL, and TiO_2-L samples. This atypical phenomenon can be attributed to the N-doped state, which prevents excessive accumulation of photogenerated carriers on surfaces and reduces depletion layer thickness, thereby hindering recombination.[5]

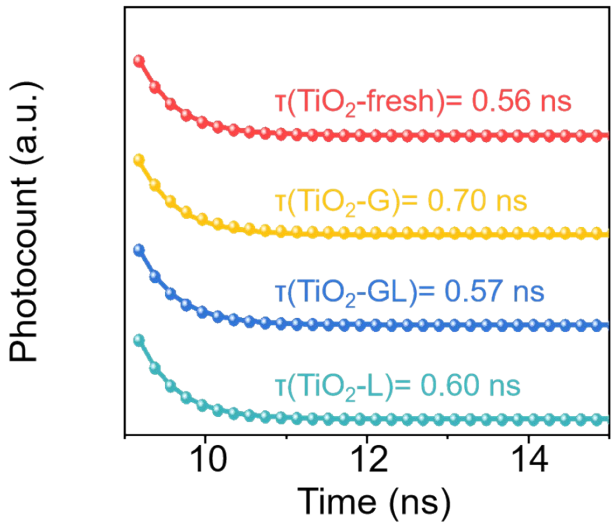

Fig. S27. TRPL spectrum of TiO_2-fresh, TiO_2-G, TiO_2-GL, and TiO_2-L.

Transient photoluminescence (TRPL) spectrum shows that the TiO_2N impedes the recombination of photogenerated electron-hole pairs, resulting in an extended exciton lifetime.

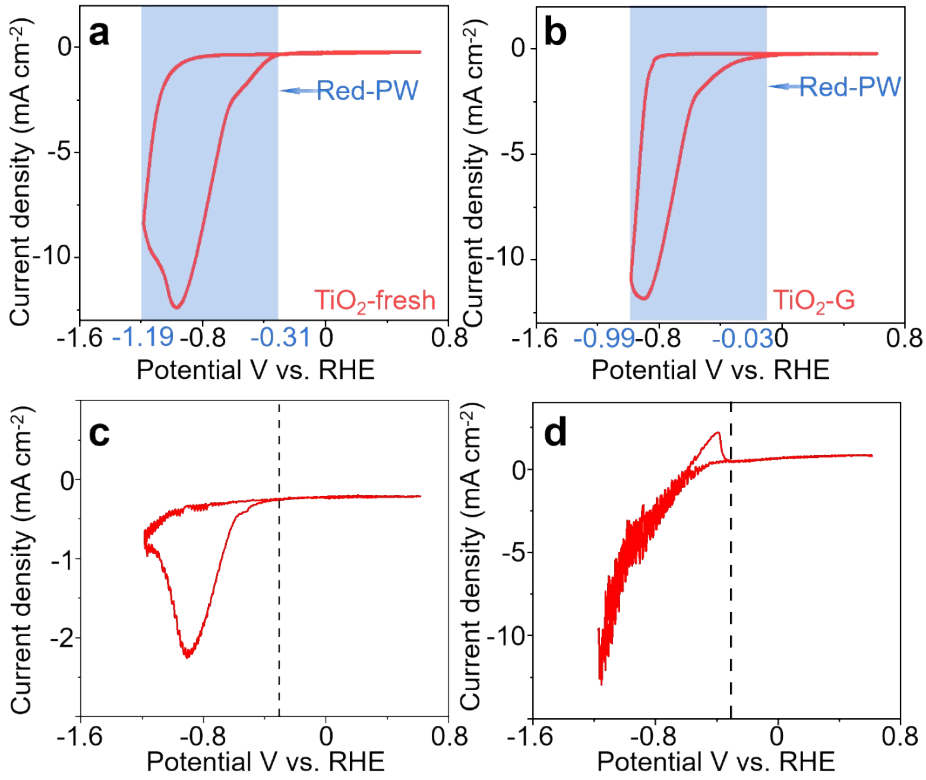

Fig. S28. CV curve of (a) TiO_2-fresh and (b) TiO_2-G in PBS. The CV curve of TiO_2 in (c) NaOH solution has a pH of 14, and (d) PBS has a pH of 7 with N_2 bubbling, respectively.

CV tests were conducted to investigate the effects of TiO_2N alterations on the redox ability through photogenerated carriers transfer at the interface.[6] The results indicate a clear shift in the catalytic reduction potential window (Red-PW) from -0.31 to -1.19 V (a) to -0.03 to -0.99 V (b). Additional tests were carried out in a NaOH solution at pH 14 under N_2 bubbling to account for the competitive reaction of hydrogen evolution and nitrogen fixation in electrocatalysis, as depicted in (c) and (d), confirming the accuracy of the CV test in representing the potential window for N_2 reduction.[7] However, the high electrical resistance of TiO_2 prevents the observation of the Oxi-PW in the CV curve.

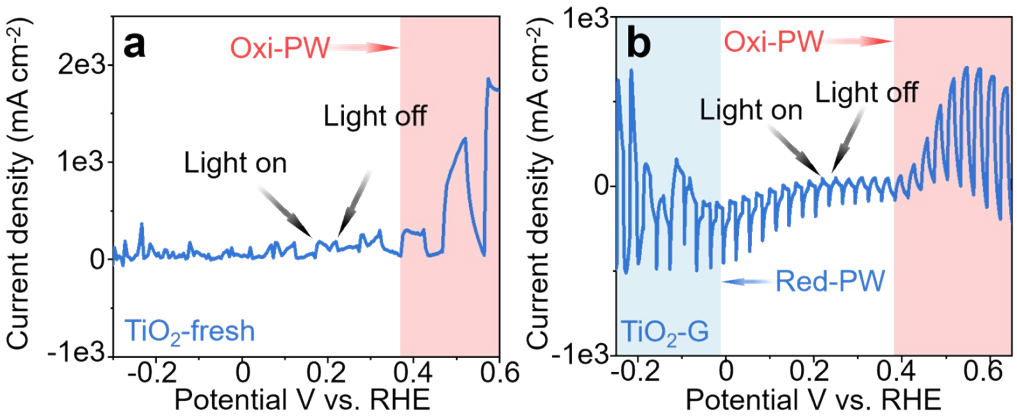

Fig. S29. LSV curve of (a) TiO_2-fresh and (b) TiO_2-G in 0.1M Na_2SO_4.

Staircase LSV tests were employed to estimate the position of the oxidation potential window (Oxi-PW), revealing a value slightly below 0.4 V.[8]

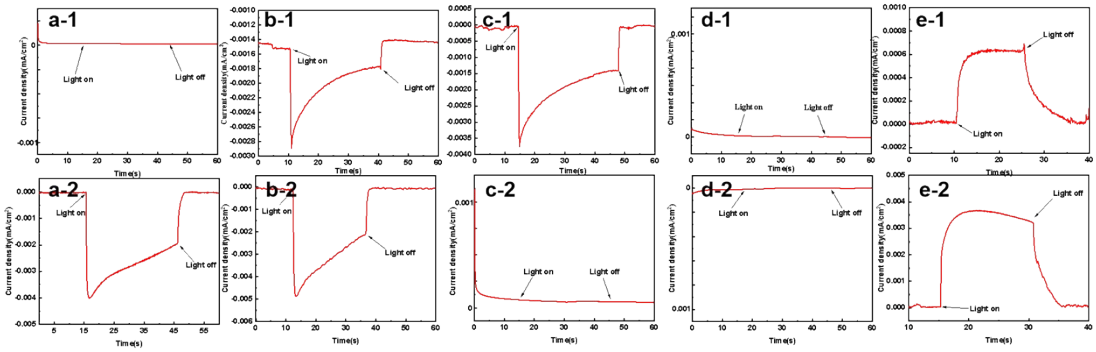

Fig. S30. Photocurrent pattern of TiO_2-G (a-1 to e-1) and TiO_2-fresh (a-2 to e-2).

To validate the change in potential windows, the voltage range of -1.25 to 1.0 V was subdivided into five regions for photovoltaic current testing. The photocurrent arises from stable oxidation or reduction reactions at the electrode. Specifically, oxidation reactions produce positive photocurrent, while reduction reactions produce negative photocurrent.[9] Additionally, the absence of reaction results in no photocurrent, thereby elucidating the role of each potential window in the specified regions.[10,11] For instance, in region a, the voltage aligns with the Red-PW of TiO_2-fresh but falls outside the Red-PW of TiO_2-G. Applying voltage within this range fails to trigger a reduction reaction in TiO_2-G, leading to a lack of photocurrent response from TiO_2-G (a-1). In contrast, a reduction reaction takes place in TiO_2-fresh, generating a negative photocurrent (a-2). Similarly, in regions (b), (c), (d), and (e), the stable photocurrent response can be observed when the applied potential falls within the Oxi-PW or Red-PW of the TiO_2.

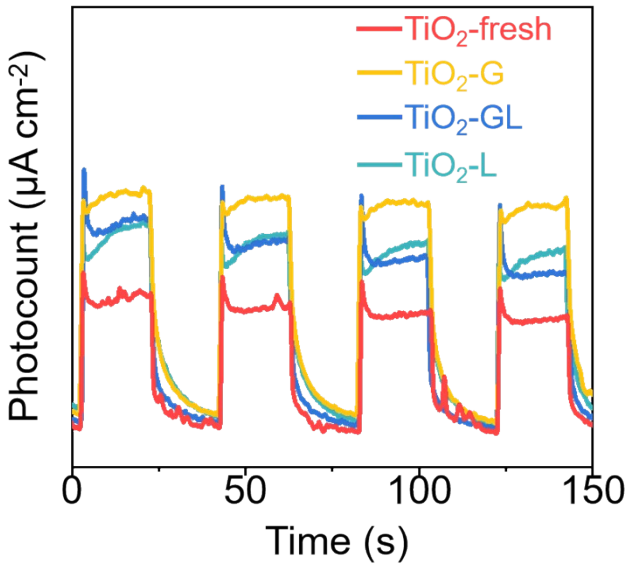

Fig. S31. Photocurrent patterns of TiO_2-fresh, TiO_2-G, TiO_2-GL, and TiO_2-L.

Based on the direct transfer theory, TiO_2 is expected to exhibit lower photocurrent and slower transfer of incident photons to electrons.[12] However, TiO_2-G shows a higher photocurrent response, proving the facilitating effect of TiO_2N on the generation of photogenerated carriers.

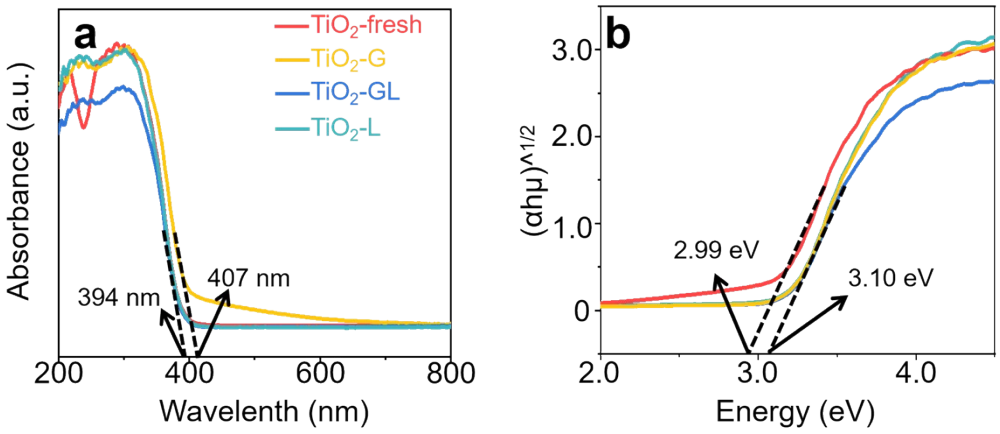

Fig. S32. DRS spectra of TiO_2-fresh, TiO_2-G, TiO_2-GL, and TiO_2-L.

The DRS analysis revealed a slight red shift in the absorption edge of TiO_2-G compared to other samples, extending the catalyst's light absorption to the visible range. The first derivative plot of DRS is depicted in (b). According to the Kubelka-Munk equation, the band gap of TiO_2-G (2.99 eV) was narrower than that of other samples (3.10 eV), which is favorable for light excitation.[13] This narrow band gap is likely due to the red shift in the absorption edge caused by TiO_2N. This result suggests that the valence band electrons in TiO_2-G are more easily excited to the conduction band for the ammonia synthesis reaction.

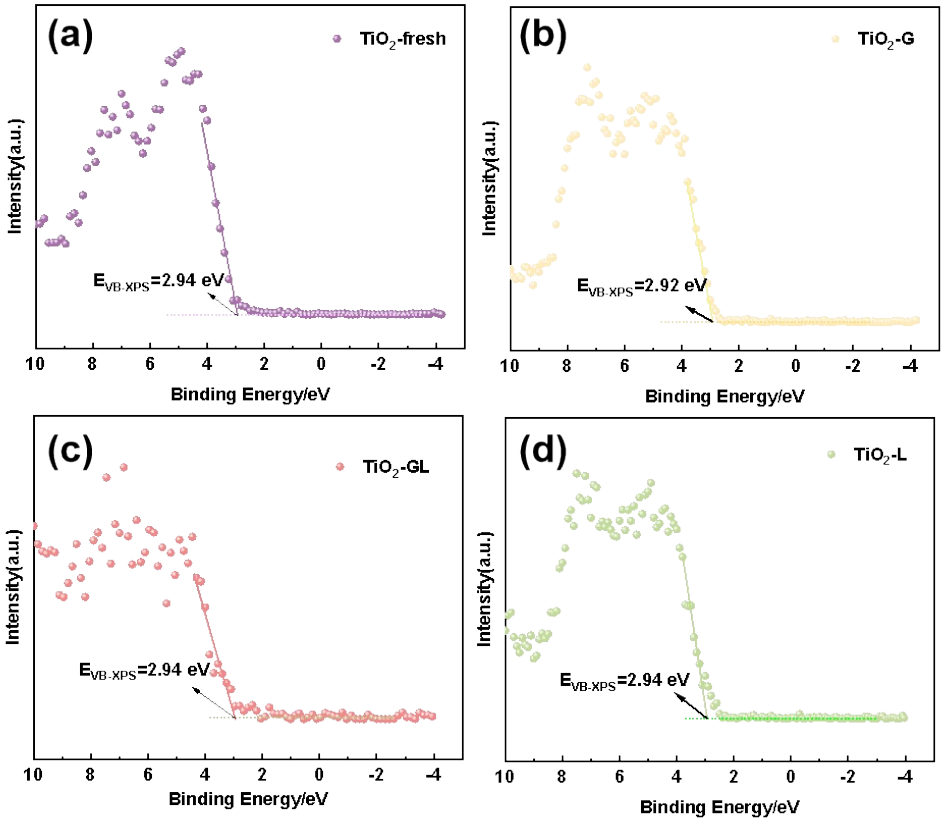

Fig. S33. VB-XPS spectrum of TiO_2-fresh, TiO_2-G, TiO_2-GL, and TiO_2-L.

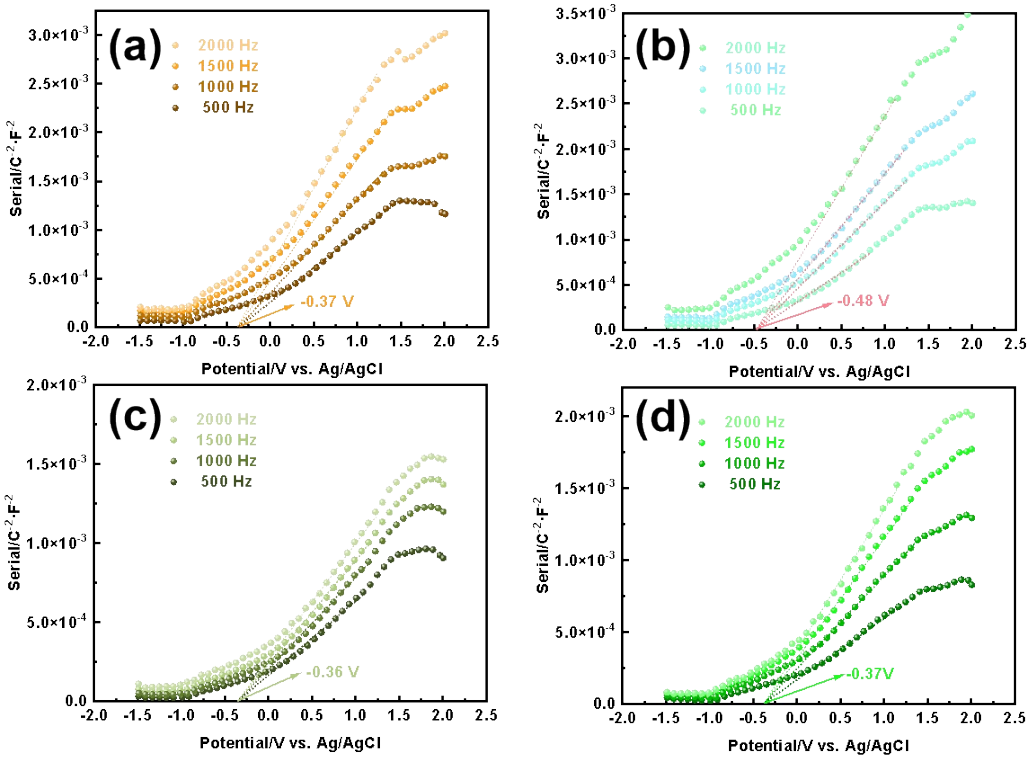

Fig. S34. MS pattern of TiO_2-fresh, TiO_2-G, TiO_2-GL, and TiO_2-L respectively.

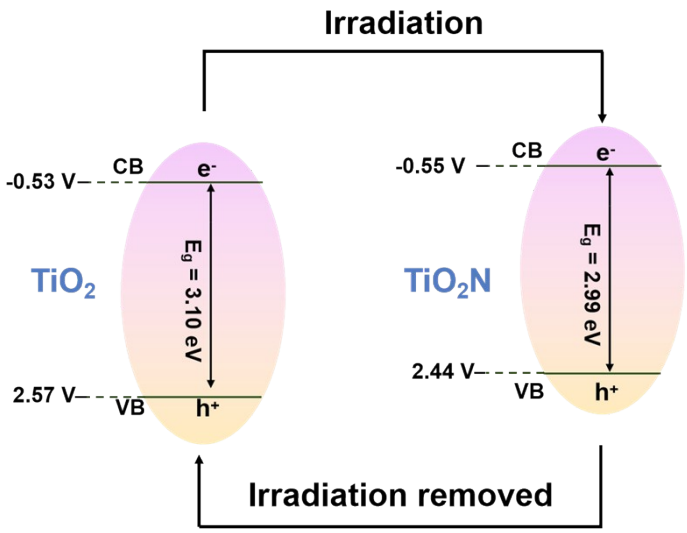

Fig. S35. Schematic illustration of the PCLAS.

By combining MS results with VB-XPS data, the band positions were determined.[14] This altered band structure can effectively enhance the rate of photocatalytic reactions.

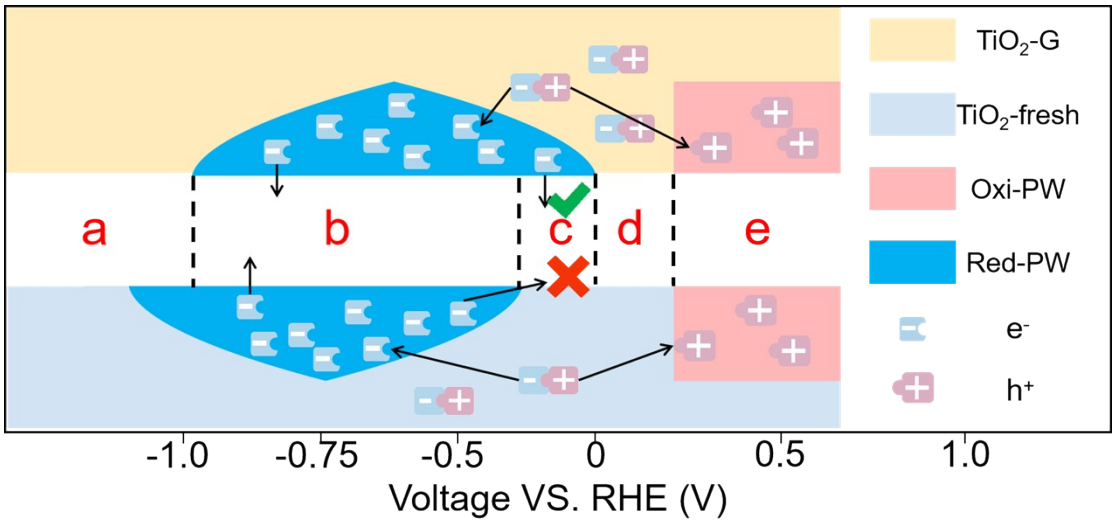

Fig. S36. Description of mechanism diagram depicting TiO_2N affecting the variation of oxidation potential window (Oxi-PW) and reduction potential window (Red-PW).

Based on the results presented in Fig. S29-S34, it can be concluded that TiO_2N optimizes the separation and transfer efficiency of photogenerated charge carriers, particularly enhancing the reduction potential window of the samples.

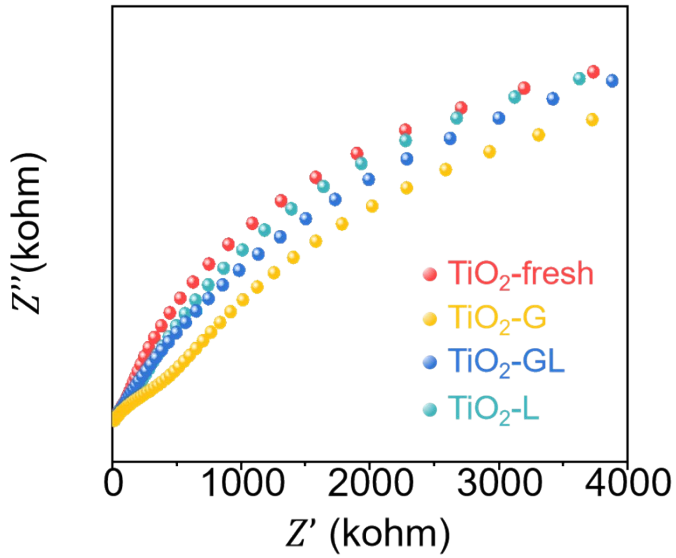

Fig. S37. EIS patterns of TiO_2-fresh, TiO_2-G, TiO_2-GL, and TiO_2-L. TiO_2-G to possess the fastest surface reaction rate.

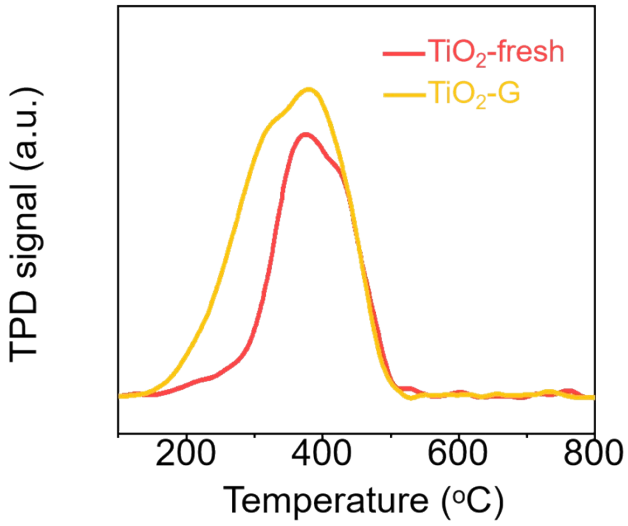

Fig. S38. N_2-TPD patterns of TiO_2-fresh and TiO_2-G.

N_2-TPD confirms that N_2 primarily adsorbs on the Ovs of the sample. Compared to TiO_2-fresh, TiO_2-G exhibits a higher chemical adsorption peak, strongly indicating that in-situ lattice strain can increase the number of N_2 adsorption sites.[15]

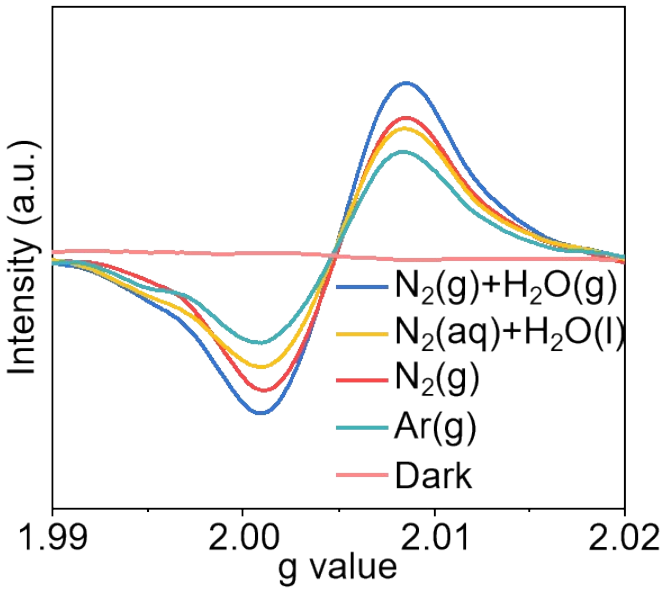

Fig. S39. EPR test of TiO_2 after reaction in different environments.

The consequence of the EPR figure shows that the signal of Ovs on the TiO_2 surface remains relatively constant under various conditions after illumination, while no signal for Ovs is detected in darkness. Consequently, it can be concluded that Ovs can be generated by light, and the changes in TiO_2 following GR and LR are not attributable to fluctuations in the concentration of Ovs.

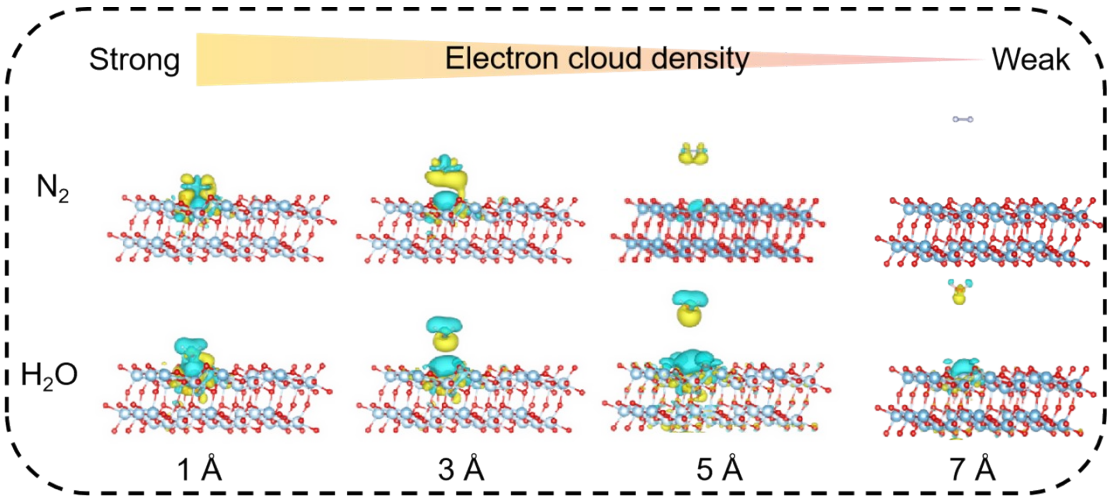

Fig. S40. The CDD calculations for N_2 and H_2O molecules at 1-7 Å from the catalyst surface were performed with an isosurface level of 0.002 for both species.

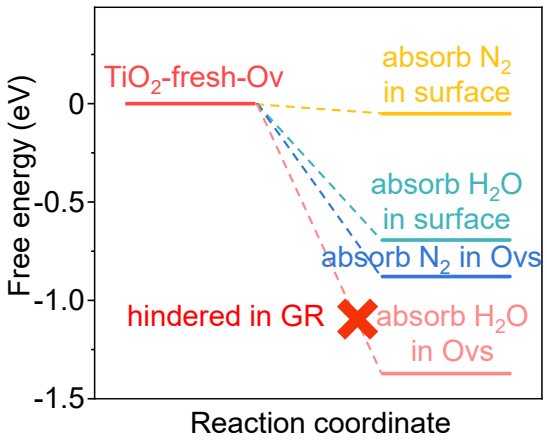

Fig. S41. Adsorption energies of N_2 and H_2O at Ovs sites on the TiO_2 surface.

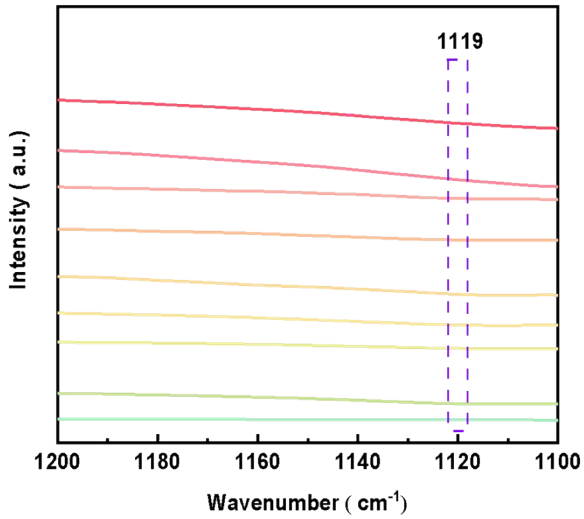

Fig. S42. Single peak of in-situ FTIR magnified image of 1119 cm^{-1}.

The hydrogenation modes of N_2 generally encompass overlapping hydrogenation and terminal hydrogenation. Overlapping hydrogenation is marked by the presence of the NH_2-NH_2 peak at 1119 cm^{-1},[16] however, the lack of a signal at this wavenumber in the in-situ FTIR measurements substantiates the occurrence of terminal hydrogenation.

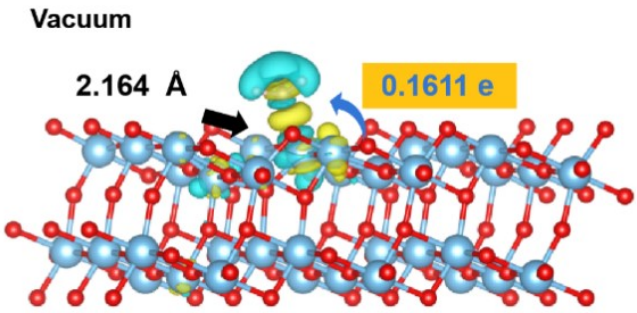

Fig. S43. CDD and Bader charge analysis of *NH_3 on the TiO_2 surface under vacuum conditions.

Under vacuum conditions, the charge delocalization on the TiO_2 surface is attenuated relative to that in the GR model, corroborating the claim that GR facilitates surface charge delocalization. Furthermore, the Ti-N bond length (2.164 Å) and the associated charge transfer from Ti to N (0.1611 e) in vacuum are nearly identical to those observed in GR (2.165 Å and 0.1639 e, respectively), yet differ markedly from the values obtained in LR (2.200 Å and 0.1540 e). These findings collectively confirm that, in the LR model, H_2O suppresses the electron-withdrawing effect of N while promoting N spillover from the TiO_2 lattice.

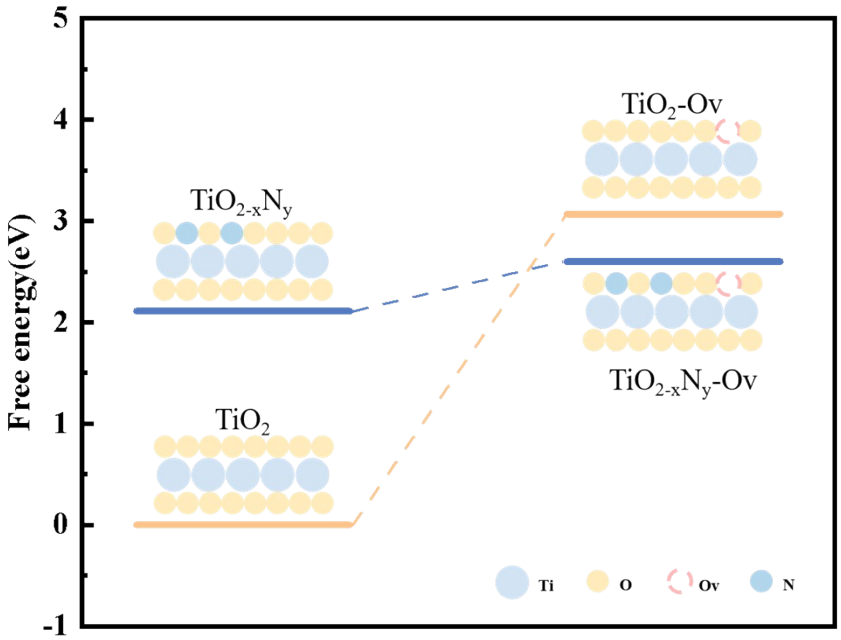

Fig. S44. The energy barrier for the regeneration of Ovs on the surfaces of TiO_2 and TiO_2N.

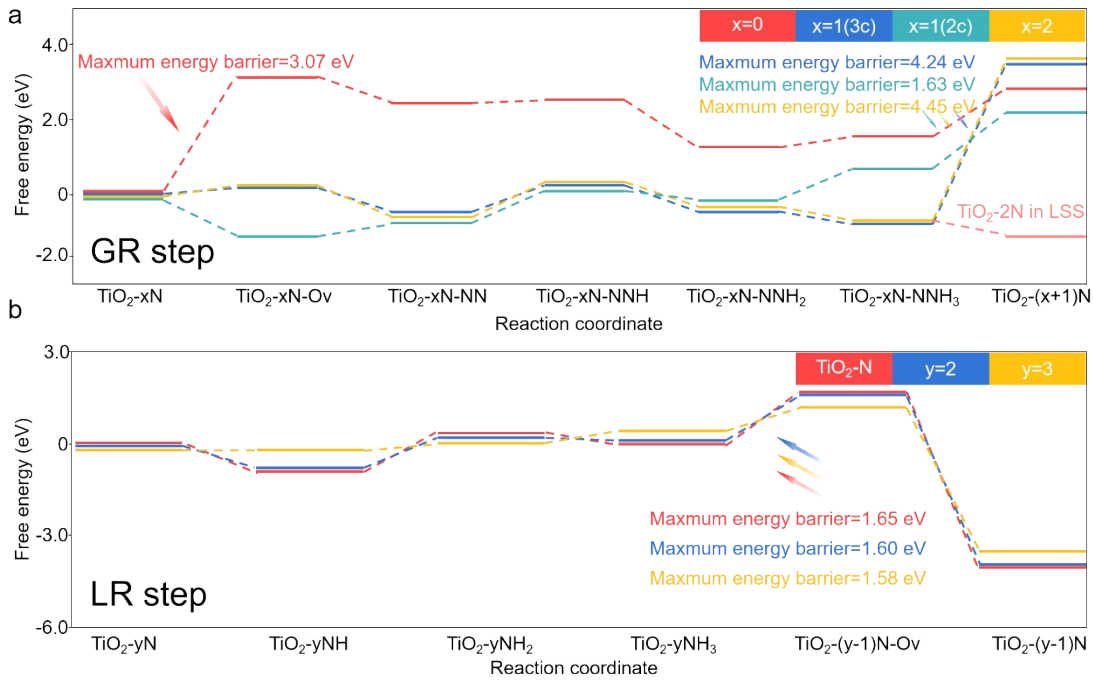

Fig. S45. (a) Nitridation reaction pathways on the TiO_2 surface in GR with 0-2 N atoms pre-adsorbed on the surface. (b) Denitridation reaction pathways on the TiO_2 surface in LR with 0-2 N atoms pre-adsorbed on the surface.

As illustrated in Fig. S45(a), the energy barrier for the initial nitridation step on the fresh TiO_2 surface originates primarily from the formation of Ovs (3.07 eV), which decreases dramatically following surface N-doping, indicating that N-doping facilitates Ovs regeneration. After the first nitridation (x = 1), the incorporation of a second N atom can occur at either three-coordinated (3c) or two-coordinated (2c) oxygen sites. The calculated barrier at the 2c site (1.63 eV) is substantially lower than that at the 3c site (4.24 eV), revealing that O atoms at 2c positions are preferentially substituted by N atoms. This finding further suggests that a mildly nitridated surface exhibits a lower doping barrier than the pristine surface, confirming the operation of a "self-accelerating N-doping cycle." Following extensive surface nitridation (x = 3), however, the doping barrier rises sharply to 4.45 eV, effectively halting further nitridation and terminating the self-accelerating cycle, consistent with the decreased activity observed after 3h in GR (Fig. 2(d)). Upon transferring the highly nitridated TiO_2 to the LR system, the reaction barrier drops to 1.58 eV, and notably, the barrier for denitridation in LR remains independent of the number of surface N atoms.

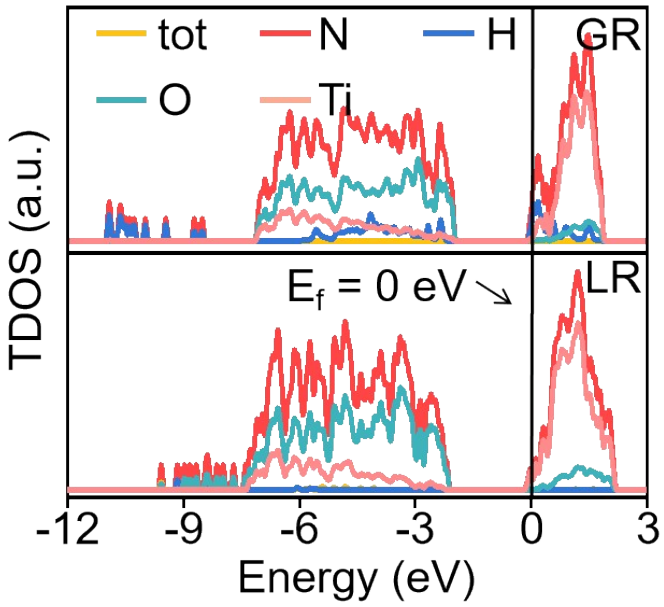

Fig. S46. Total DOS pattern of N-doped TiO_2 in GR and LR.

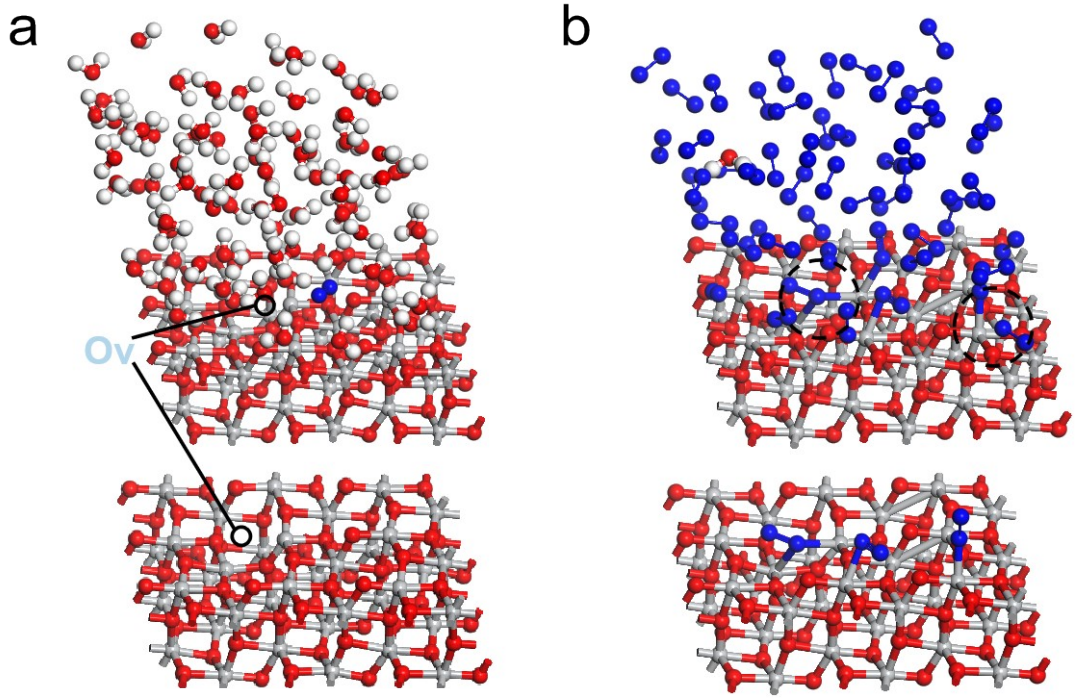

Fig. S47. MD structure of (a) LR, and (b) GR.

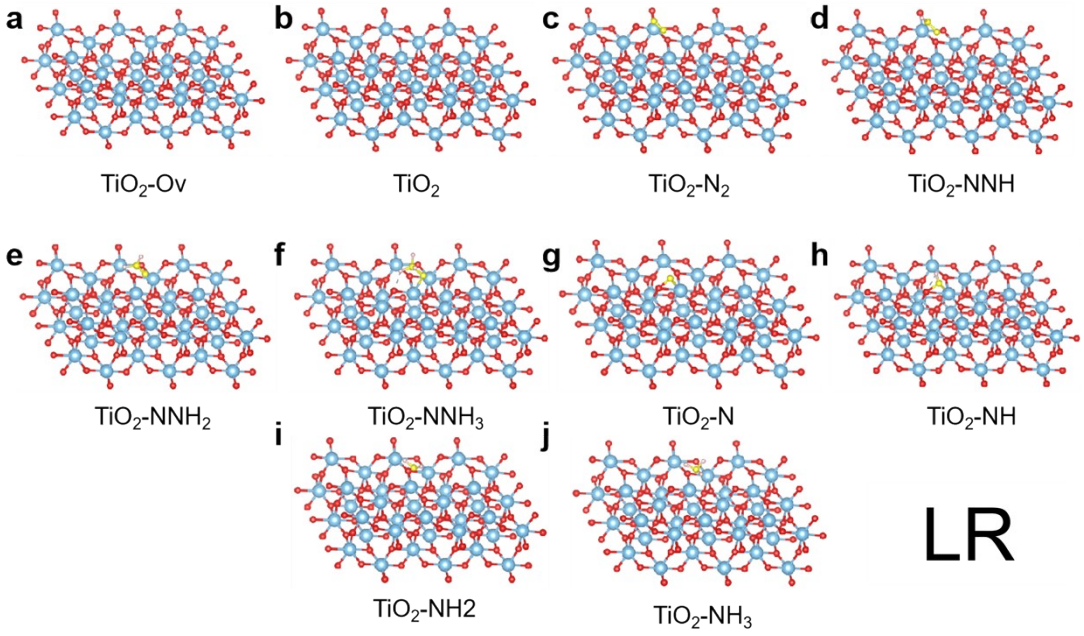

Fig. S48. Computational models of LR.

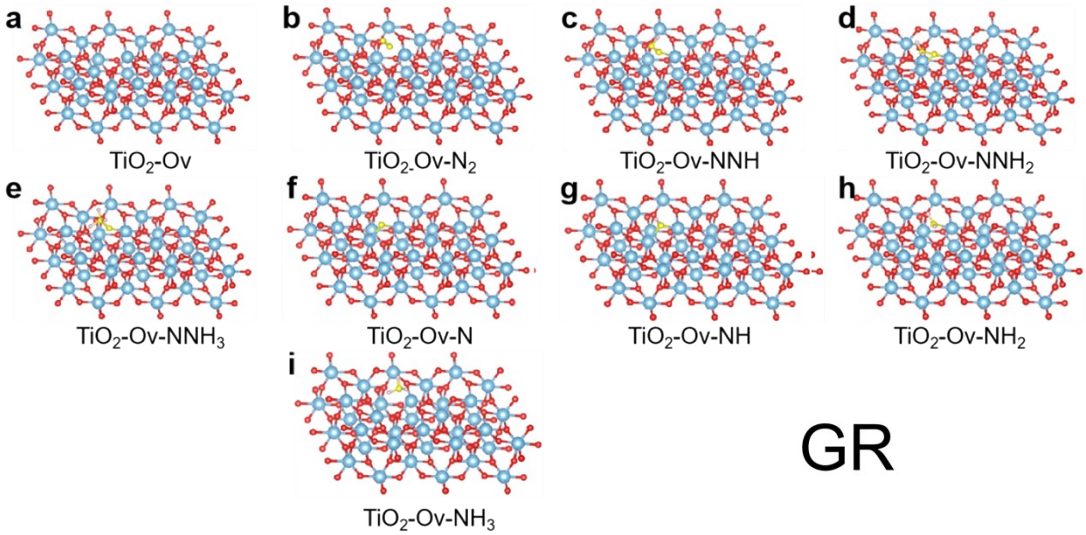

Fig. S49. Computational models of GR.

9. Supporting Table

Table S1. The activities and operation temperatures for some existing non-noble-metal photocatalytic ammonia synthesis processes.

Photocatalytic system	**Reaction conditions (light source, temperature, and dosage)**	**NH_3 productivity (mmol g^{-1} h^{-1})**	**Ref.**
CdS/MIL-68(Fe)	λ > 400 nm, 25 ℃, 10 mg	0.05	17
BiOBr/$Bi_4O_5Br_2$	λ > 420 nm, 25 ℃, 50 mg	0.07	18
Mo[$PMo_{12}O_{40}$]	full spectrum, 25 ℃, 10 mg	0.10	19
Bi_2WoO_6	full spectrum, 30 ℃, 50 mg	0.17	20
Bi/$Bi_2Sn_2O_7$	full spectrum, 25 ℃, 20 mg	0.28	21
NH_2-MIL-101(Fe, Co)	λ > 420 nm, 25 ℃, 30 mg	0.34	22
Cu_2O/TiO_2/NiO	full spectrum, 25 ℃, 100 mg	0.34	23
$Bi_4O_5Br_2$/$CdWO_4$	λ > 420 nm, 25 ℃, 100 mg	0.50	24
Fe/$FaTiO_2$	full spectrum, 25 ℃, 10 mg	0.78	25
CeO_2-CZH	full spectrum, 25 ℃, 100 mg	0.99	26
TiO_2, PCLAS	full spectrum, 25 ℃, 4 mg	1.48	This work

Table S2. The activities and operation temperatures for some existing CLAS processes.

N carrier pairs	Operation condition		NH_3 productivity (mmol g^{-1} h^{-1})	Ref.
	Nitridation step (℃)	Denitridation step (℃)		
ZrO_2-AlN/Al_2O_3	1000	1000	0.82	27
P-Si_x-Y_y-γ-Al_2O_3	750*	750	0.38	28
LiH/Li_2NH	350	350	0.96	29
Fe-BaH_2/Fe-BaNH	300	300	1.70	30
Ta/Ta_3N_5	700	400	0.08	31
Mo-ZSM-5/Mo_2N-ZSM-5	600	600	0.75	32
Co_6Mo_6N/Co_3Mo_3N	700	500	0.16	33
E-LiH/Li_2NH	400**	400	2.06	34
P-MgO-NaH/$NaNH_2$	300***	25	0.55	35
TiO_2/N-doped TiO_2	25	25	1.48	This work

*Applied voltage: 2 kV. **Applied voltage: 2 V. ***Applied voltage: 12 kV.

Table S3. The reaction conditions and STA efficiency for some existing photocatalytic reactions.

Photocatalytic system	**Reaction conditions**	**STA efficiency (%)**	**Ref.**
JRC-TIO-6	280-420 nm	0.02	36
MWO-1 UTNWs	full spectrum	0.028	37
Bi_2O_3@CoAl-LDHs	$\lambda > 400$ nm	0.0013	38
SWMO0.1	full spectrum	0.035	39
MoO_{3-x}	$\lambda > 400$ nm	0.3	40
Ag/AAO	200 ℃, 0.4 MPa, 575 nm	0.15	41
TiO_2, PCLAS	full spectrum	0.40	This work

Table S4. The yield and AQY for some existing photocatalytic reactions.

Photocatalytic system	**Light wavelength (nm)**	**Yield (mmol g^{-1} h^{-1})**	**AQY (%)**	**Ref.**
g-C_3N_4/MoFeTiO	450	0.76	4.10	42
TiO_2	365	0.32	1.10	43
C-defect-CoP_4	365	1.25	3.51	44
BiOBr/HCC	400	0.20	0.22	45
SiP/NSs	420	0.04	3.56	46
$Bi_4O_5Cl_2$-$Bi_4O_5Br_2$	420	0.25	0.34	47
Bi/BiOBr	400	0.38	0.0248	48
TiO_2, PCLAS	400	1.48	5.31	This work

Table S5. Photocatalytic activity measured over a 4h GR reaction period (unit: mmol g^{-1} h^{-1}, reported to four significant figures).

Reaction time	Replicate 1	Replicate 2	Replicate 3	Average
1	0.5532	0.5725	0.5608	0.5640
2	1.498	1.663	1.679	1.680
3	1.914	1.998	1.876	1.886
4	1.918	2.193	2.063	2.078

Table S6. Photocatalytic activity measured over a 4h LR reaction period (unit: mmol g^{-1} h^{-1}, reported to four significant figures).

Reaction time	Replicate 1	Replicate 2	Replicate 3	Average
1	0.03822	0.03813	0.03585	0.03646
2	0.06699	0.07300	0.07134	0.7044
3	0.0950	0.1053	0.1020	0.1007
4	0.1302	0.1355	0.1324	0.1330

Table S7. Photocatalytic activity measured over a 2h GR + 2h LR reaction period (unit: mmol g^{-1} h^{-1}, reported to four significant figures).

Reaction time	Replicate 1	Replicate 2	Replicate 3	Average
1(GR)	0.5279	0.7064	0.6152	0.6297
2(GR)	1.592	1.882	1.724	1.752
3(LR)	3.140	3.967	3.546	3.621
4(LR)	5.969	5.822	6.139	5.992

Table S8. Nitrogen content of eleven transition metal oxides under fresh, after nitridation (GR), and after denitridation (LR).

Metal oxides	**Nitrogen content (fresh, %)**	**Nitrogen content (After nitridation, %)**	**Nitrogen content (After denitridation, %)**
MoO_3	0.0082	0.0283	0.0035
NiO	0.0021	0.0026	0.0023
ZrO_2	0.0012	0.0022	0
Y_2O_3	0.0009	0.0087	0
Gd_2O_3	0.0053	0.0064	0
Bi_2O_3	0	0.0018	0
Co_3O_4	0.0111	0.0179	0.0062
CuO	0.0016	0.0064	0.0034
In_2O_3	0	0	0
MgO	0.0123	0.0127	0.0099
TiO_2	0	0.0512	0

10. References

[1] A. Takahashi, H. Tanaka, D. Parajuli, T. Nakamura, K. Minami, Y. Sugiyama, Y. Hakuta, S. Ohkoshi and T. Kawamoto, *J. Am. Chem. Soc.,* 2016, **138**, 6376-6379.

[2] Y. Zhao, Y. Zhao, R. Shi, B. Wang, G. Waterhouse, L. Wu, C. Tung and T. Zhang, *Adv. Mater.,* 2019, **31**, 1806482.

[3] G. Zhang, X. Yang, C. He, P. Zhang and H. Mi, *J. Mater. Chem. A,* 2020, **8**, 334.

[4] Q. Liang, M. Zhang, Z. Zhang, C. Liu, S. Xu and Z. Li, *J. Alloy. Compd.,* 2017, **690**(5), 123-130.

[5] W. Zhang, J. Zhao, Z. Liu, Z. Liu and Z. Fu, *Appl. Surf. Sci.,* 2010, **256**(14), 4423-4425.

[6] Q. Ruan, X. Xi, B. Yan, L. Kong, C. Jiang, J. Tang and Z. Sun, *Chem,* 2023, **9**, 1-15.

[7] H. Dong, X. Pan, Y. Gong, M. Xue, P. Wang, S. Ho-Kimura, Y. Yao, H. Xin, W. Luo and Z. Zou, *Nat. Commun.,* 2023, **14**, 1969.

[8] M. Chen, H. Dong, M. Xue, C. Yang, P. Wang, Y. Yang, H. Zhu, C. Wu, Y. Yao, W. Luo and Z. Zou, *Nat. Commun.,* 2021, **12**, 6363.

[9] P. Wang, M. Xue, D. Jiang, Y. Yang, J. Zhang, H. Dong, G. Sun, Y. Yao, W. Luo and Z. Zou, *Nat. Commun.,* 2022, **13**, 2544.

[10] M. Xue, Z. Chu, D. Jiang, H. Dong, P. Wang, G. Sun, Y. Yao, W. Luo and Z. Zou, *Natl. Sci. Rev.,* 2023, **10**(4), nwac249.

[11] P. Wang, X. Chen, G. Sun, C. Wang, J. Luo, L. Yang, J. Lv, Y. Yao, W. Luo and Z. Zou, *Angew. Chem. Int. Ed.,* 2021, **60**, 1390-1395.

[12] C. Chen, M. Wu, Y. Xu, C. Ma, M. Song and G. Jiang, *J. Am. Chem. Soc.,* 2024, **146**(13) 9163-9171.

[13] S. Karmakar, K. L. Routray, B. Panda, B. Sahoo and D. Behera, *J Alloy. Compd.,* 2018, **765**, 527-537.

[14] Q. Zhang, H. Zhang, B. Gu, Q. Tang, Q. Cao and W. Fang, *Appl. Catal. B-Environ. Energy,* 2023, **320**, 122066.

[15] M. Watanabe, Y. Aizawa, T. Iida, R. Nishimura and H. Inomata, *Appl. Catal. A-Gen.,* 2005, **295**(2), 150-156.

[16] X. Dong, X. Shi, Z. Cui, W. Dai and F. Dong, *ACS Nano,* 2024, **18**, 9670-9677.

[17] Q. Chen, Z. Zhang, Y. Chen, J. Yu, C. Liu and L. Wu, *Appl. Catal. B-Environ. Energy.,* 2026, **380**, 125823.

[18] H. Wang, Z. Chen, Y. Shang, C. Lv, X. Zhang, F. Li, Q. Huang, X. Liu, W. Liu, L. Zhao, L. Ye, H. Xie and X. Jin, *ACS Catal.,* 2024, **14**(8), 5779-5787.

[19] X. Gong, W. Teng, W. Liu, H. Xiao, H. Li, H. Ou and G. Yang, *Adv. Mater.,* 2025, **37**(3), 2412924.

[20] X. Huang, R. Du, J. Ren, X. Li, M. Fu, S. Fu, T. Ma, L. Guo, R. A. Soomro, C. Yang and D. Wang, *ACS Catal.,* 2024, **14**(18), 13542-13549.

[21] R. Wu, S. Gao, C. Jones, M. Sun, M. Guo, Ran. Tai, S. Chen and Q. Wang, *Adv. Funct. Mater.,*2024, **34**(24), 2314051.

[22] H. Feng, Q. Xu, T. Lv and H. Liu, *Appl. Catal. B-Environ. Energy.,* 2024, **351**, 123949.

[23] X. Lu, J. Hu, X. Jiang, J. Li, Z. Lu, J. Xie and Y. Cao, *Adv. Funct. Mater.,* 2025, **35**(32), 2502690.

[24] C. Zhao, X. Li, L. Yue, X. Ren, S. Yuan, Z. Zeng, X. Hu, Y. Wu and Y. He, *ACS Appl. Nano Mater.,* 2023, **6**(17), 15709-15720.

[25] X. Ge, X. Zheng, T. Zhou, L. Tian, W. Wang, J. Chen and X. Wang, *Angew. Chem. Int. Ed.,* 2025, **137**(40), e202506470.

[26] H. Zhang, L. Bao, Y. Pan and J. Ge, *Sol. Energy,* 2023, **264**, 112002.

[27] Y. Wu, Y. Gao, Q. Zhang, T. Cai, X. Chen and D. Liu, *Fuel*, 2020, **264**, 116821.

[28] Y. Zhang, H. Qin, Y. Long, A. Cao, K. Wang and L. Gao, *Appl. Catal B Environ.* 2025, **371**, 125206.

[29] R. Wang, W. Gao, S. Feng, Y. Guan, Q. Wang and J. Guo, *Chem. Sus. Chem.*, 2023, **16**, e202300813.

[30] W. Gao, J. Guo, P. Wang, Q. Wang, F. Chang and Q. Pei, *Nat. Energy*, 2018, **3**, 1067-1075.

[31] A. M. Alexander, J. S. J. Hargreaves and C. Mitchell, *Top Catal*, 2012, **55**, 1046-1053.

[32] M. Zhang, F. Guan, T. Guo, M. Wu and Q. Guo, *Int. J. Hydrogen Energy*, 2025, **120**, 497-506.

[33] D. McKay, D. H. Gregory, J. S. J. Hargreaves, S. M. Hunter and X. Sun, *Chem. Commun.*, 2007,3051-3053.

[34] S. Feng, W. Gao, J. Guo, H. Cao and P. Chen, *ACS Energy Lett.*, 2023, **8**, 1567-1574.

[35] H. Wu, L. Yang, J. Wen, Y. Xu, Y. Cai and W. Gao, *Adv. Energy Mater.*, 2023, **13**, 2300722.

[36] J. Li, Y. Zhang, C. Liu, L. Zheng, E. Petit, K. Qi, Y. Zhang, H. Wu, W. Wang, A. Tiberj, X. Wang, M. Chhowalla, L. Lajaunie, R. Yu and D. Voiry, Adv. Funct. Mater., 2022, 32(18), 2108316.

[37] Y. Shiraishi, S. Shiota, Y. Kofuji, M. Hashimoto, K. Chishiro, H. Hirakawa, S. Tanaka, S. Ichikawa and T. Hirai, ACS Appl. Energy Mater., 2018, 1(8), 4169-4177

[38] Y. Jin, K. Lin, H. Liu, Z. Zhou, X. Mao, Y. Men, W. N. Martens, T. Tesfamichael, S. Sarina, E. R. Waclawik, A. Du, H. Lin, B. Jia, S. E. Bottle and H. Zhu, J. Am. Chem. Soc. 2026,

doi.org/10.1021/jacs.5c22728.

[39] Y. Li, M. Duan, S. S. Wu, T. A. Taylor and S. C. E. Tsang, Adv. Energy Mater. 2026, 16, 2406160.

[40] T. Liu, Y. Huang, Y. Huang, Y. Lu, T. Tsai, C. Chang, P. Kuo, J. Shiue, Y. Huang, C. Chen, C. Chen and S. Li, J. Mater. Chem. A, 2025,13, 12104-12112.

[41] J. Ding, Y. Lyu, H. Zhou, B. Johannessen, X. Zhang, J. Zheng, S. P. Jiang and S. Wang, Appl. Catal. B-Environ. Energy, 2024, 345, 123735.

[42] H. Li, L. Yang, S. Wu, J. Zhang, Z. Shao, Y. Zhou, D. Zhang and P. Li, *Chem. Eng. J.*, 2026, **528**, 172637.

[43] G. Zhang, X. Yang, C. He, P. Zhang and H. Mi, *J. Mater. Chem. A*, 2020, **8**, 334-341.

[44] X. Wang, Y. Zhao, X. Wu, B. Zhang, J. Tian, W. Wong and F. Zhang, *Angew. Chem. Int. Edit.*, 2025, **137**(8), e202420327.

[45] X. Wang, Y. Li, L. Feng, Y. Yang and X. Zheng, *Small*, 2025, **21**(39), e03853.

[46] Y. Yuan, N. Lu, L. Bao, F. Zhang, J. Guan, H. Wang, Q. Liu, Q. Cheng, Z. Yu and Z. Zou, *ACS Nano*, 2022, **16**(8), 12174-12184.

[47] Q. Luo, X. Deng, T. Zhao, S. Yin and P. Chen, *Nano Lett.*, 2025, **25**(6), 2493-2501.

[48] X. Zheng, X. Wang, L. Feng, Z. Chen, J. Zhang, X. Zhang and P. Liu, *ACS Appl. Mater. Interfaces*, 2024, **16**(45), 62107-62120.